von Karman Institute for Fluid Dynamics

Lecture Series 2025-01

MEASUREMENT, MODELLING AND SIMULATIONS TECHNIQUES FOR NOVEL AIRCRAFT ARCHITECTURES

November 4-6, 2024

SCALE-RESOLVED AEROACOUSTIC SIMULATIONS OF PROPULSION SYSTEMS

M. Meinke, A. Niemöller, M. Gondrum, Z. Yang
Institute of Aerodynamics, RWTH Aachen University, Germany

1 Introduction

Aeroacoustics as the study of noise generated by unsteady fluid flow, in particular due to the interaction of turbulent flow with solid surfaces, occurs for aircraft, automotive vehicles, or in turbomachinery. Predicting and mitigating aeroacoustic noise is crucial in many industries, including aerospace, automotive, and wind energy, where noise reduction is a key design goal. To understand and predict noise levels and sources accurately, engineers and scientists rely on computational methods that simulate details of turbulent flows, and the interaction of such flows with the structures that generate sound. This involves the use of computational fluid dynamics (CFD) methods, for which one important ingredient is the turbulence modeling. As a very rough distinguishing criterion, turbulence scale resolving simulations (SRS) can be differentiated from simulations based on the Reynolds averaged Navier-Stokes equations (RANS). For accurate aeroacoustic predictions without introducing further modelling assumptions, it is necessary to resolve the key flow features responsible for noise generation. Aeroacoustic noise is often generated by turbulent boundary layers interacting with solid surfaces e.g. producing trailing edge noise. In free shear layers or separated flows, particularly around blunt bodies, the flow field with unsteady vorticity will generate noise. Examples are flows around complex geometries, such as landing gears or high lift components.

SRS refers to a family of computational fluid dynamics techniques that aim to capture a broad range of turbulent flow scales. The core idea behind SRS is that turbulence, which plays a dominant role in aeroacoustics, exists over a range of scales, i.e. from large eddies down to the smallest turbulent structures. Accurately resolving these scales is essential for capturing the intricate dynamics that produce sound in many applications. In SRS, we have a hierarchy of methods ranging from detached eddy simulations (DES) to Large Eddy Simulation (LES) and Direct Numerical Simulation (DNS). DNS resolves all scales of turbulence directly without any modeling, which is, however, generally too expensive due to the high mesh resolution requirements and the associated computational expense for high Reynolds number flow. In LES, the larger turbulent scales are captured, while the smaller subgrid scales are modelled. It provides a more detailed and accurate prediction of the flow and noise generation, but typically at a higher computational cost than RANS. DES methods try to combine the efficiency of RANS models close to solid boundaries and the accuracy of LES in the regions of free turbulence such as wakes. This approach is often used in aeroacoustic applications, because it can provide a balance between accuracy and computational cost. Other approaches to reduce the computational effort is to apply wall-modelled LES (WMLES), where the near wall region is not resolved, but a wall function for the velocity distribution is used. Further modelling approaches include zonal or hybrid RANS-LES, in which the domain is split into distinct regions, which are then predicted either by RANS or LES methods, coupled through appropriate boundary conditions. For all such turbulence modelling approaches many variants exist, which will not be further discussed in this paper. The focus will be on turbulence scale resolving methods used in the context of aeroacoustic applications and the methods used to determine the acoustic field. In more detail, two representative CFD methods will be applied, the first is based on a finite-volume solver for the Navier-Stokes equations and the second on a lattice Boltzmann method, both are used to perform LES of turbulent flow fields.

SRS methods are commonly applied in aircraft related noise prediction, e.g. to simulate the noise produced by landing gears, flaps, and jet engines. For stationary geometries many mature methods already exist for the noise prediction. For rotating components such as propellers or fans another difficulty is the tracking of rotating components, for which also a variety of methods exists. One technique to resolve rotating components relative to each other are based on multiple frames of reference, where e.g. a rotating frame of reference is used around the propeller and a fixed reference frame for the domain with stationary objects. To obtain a smooth transition between the reference frames, sliding interfaces or chimera or overset meshes involving interpolation have to be applied. Another solution technique makes use of immersed boundaries, where e.g. the rotating blades move through a fixed Cartesian mesh. Of the various available methods, the method using an immersed boundary formulation for a Cartesian mesh, which involves dynamic mesh adaption for the moving solid boundaries will be used for the cases presented in this paper. The benefit of this method is that mesh generation can be fully automatic and the hierarchical mesh allows for an efficient local mesh adaption.

One of the big challenges in the application of SRS methods like LES, is the requirement for significant computational resources on high performance computing (HPC) systems. Reducing computational costs without sacrificing accuracy is still a key research focus. Another challenge is connected to the coupling of the flow field with acoustic propagation models. The prediction of the noise at a far-field observer requires coupling the flow simulation with acoustic propagation models, such as the Ffowcs Williams-Hawkings (FW-H) or the acoustic perturbation equations, to translate near-field noise into far-field noise predictions. Here, the coupling of the various methods on HPC systems can still be a tedious, if commercial solutions are not available. Here, two CFD solvers either directly coupled to a computational aeroacoustics (CAA) solver or to a FW-H method will be used.

In this paper, an overview is given, which shows how SRS methods can be used to predict aeroacoustic problems. Details of several use cases are presented, which demonstrate how SRS can be used to accurately predict the acoustic field. After the introduction of the mathematical formulations for the selected CFD and CAA methods in section 2 and the numerical methods in section 3, several use cases will be used to illustrate the applicability of these methods in section 4. Finally, noise predictions for propulsion systems will be shown in section 4.4, which are based on the application of a finite-volume method for the Navier-Stokes equations coupled to a FW-H method. All results shown, are based on the application of the software framework m-AIA, which has been recently published as an open source project Institute of Aerodynamics, RWTH Aachen University 2024a. All setups for the use cases discussed in this paper, will be uploaded to the git repository Institute of Aerodynamics, RWTH Aachen University 2024b.

2 Mathematical Models

2.1 Navier-Stokes Equations

The dynamics of a compressible, viscous fluid are governed by the conservation laws of mass, momentum, and energy, which are formulated as the Navier-Stokes equations. These equations can be expressed in a non-dimensional form for a fixed control volume V within the arbitrary Lagrangian-Eulerian (ALE) framework as follows:

$$\frac{d}{dt}\int_V \boldsymbol{Q}\, dV + \oint_{\partial V} \left(\underline{\boldsymbol{F}}^{\text{inv}} + \underline{\boldsymbol{F}}^{\text{vis}}\right) \cdot \boldsymbol{n}\, d\Gamma = \mathbf{o}\ . \tag{1}$$

Here, $\Gamma = \partial V$ denotes the volume surface, with the outward-pointing normal vector $\boldsymbol{n}$. The vector of conservative variables is represented as $\boldsymbol{Q} = [\rho, \rho\boldsymbol{u}, \rho E]^T$, which includes the fluid density ρ, the velocity vector $\boldsymbol{u}$, and the specific total energy per unit mass E. The inviscid flux tensor is denoted as $\underline{\boldsymbol{F}}^{\text{inv}}$, while the viscous flux tensor is indicated as $\underline{\boldsymbol{F}}^{\text{vis}}$, given by:

$$\underline{\boldsymbol{F}}^{\text{inv}} + \underline{\boldsymbol{F}}^{\text{vis}} = \begin{bmatrix} \rho\boldsymbol{u} \\ \rho\boldsymbol{u}\boldsymbol{u} + p\underline{\boldsymbol{I}} \\ \rho E\boldsymbol{u} + p\boldsymbol{u} \end{bmatrix} + \frac{1}{Re_0}\begin{bmatrix} 0 \\ \underline{\boldsymbol{\tau}} \\ \underline{\boldsymbol{\tau}}\boldsymbol{u} + \boldsymbol{q} \end{bmatrix}, \tag{2}$$

with the pressure p and the unit tensor $\underline{\boldsymbol{I}}$. All equations are non-dimensionalized using the stagnation state properties, denoted by the index $(\cdot)_0$. Dimensional variables are indicated by $\overline{(\cdot)}$. The Reynolds number is defined as $Re0 = \frac{\overline{\rho_0}, \overline{a_0}, \overline{L}}{\overline{\mu_0}}$, based on the reference values at rest, where the speed of sound is given by $\overline{a_0} = \sqrt{\gamma, \frac{\overline{p_0}}{\overline{\rho_0}}}$, with the heat capacity ratio for air being $\gamma = 1.4$ and the characteristic length of the problem denoted as $\overline{L}$. Assuming a Newtonian fluid with zero bulk viscosity, the stress tensor $\underline{\boldsymbol{\tau}}$ is expressed as follows:

$$\underline{\boldsymbol{\tau}} = \frac{2}{3}\mu(T)\left(\nabla\cdot\boldsymbol{u}\right)\underline{\boldsymbol{I}} - \mu(T)\left(\nabla\boldsymbol{u} + (\nabla\boldsymbol{u})^T\right), \tag{3}$$

in which the dynamic viscosity $\mu(T)$ is determined by Sutherland's Law

$$\mu(T) = T^{3/2}\frac{1 + \overline{S}/\overline{T_0}}{T + \overline{S}/\overline{T_0}}. \tag{4}$$

The constant $\overline{S} = 111, \mathrm{K}$ is applicable for air at moderate temperatures. The heat flux, as defined by Fourier's law with a constant Prandtl number of $Pr_0 = 0.72$ for air, is expressed as follows:

$$\boldsymbol{q} = -\frac{\mu(T)}{Pr_0(\gamma - 1)}\nabla T. \tag{5}$$

The system of equations is closed with the ideal gas law in non-dimensional form $\gamma p = \rho T$.

Boundary Conditions On rigid surfaces, the no-slip condition is applied, meaning the velocity vector is equal to the velocity of the surface. In simulations involving moving objects, the velocity is set to match the local object velocity. It is assumed that the surface of the object is adiabatic, and a Robin-type pressure boundary condition is used, which is derived from the momentum equation in the surface-normal direction. In the far field, non-reflecting inflow/outflow conditions are enforced, along with a sponge layer to minimize spurious reflections of pressure waves. For further details, see Schneiders, Günther, et al. 2016; Fröhlich et al. 2021.

2.2 Boltzmann Equation

The Boltzmann equation governs the temporal evolution of the particle probability density function (PPDF), denoted as $f(\vec{x}, \vec{\xi}, t)$. This function represents the likelihood of locating a particle at a specific position in momentum space, namely, near position $\vec{x}$ at time t with a particle velocity $\vec{\xi}$. The Boltzmann equation can be written as follows:

$$\frac{\partial f}{\partial t} + \vec{\xi} \cdot \nabla_x f + \frac{\vec{F}}{\rho} \cdot \nabla_\xi f = \Omega(f)\,, \tag{6}$$

Here, $\vec{F}$ represents an external force, and the collision operator Ω accounts for the impact of particle collisions on the momentum distribution function. Through a series expansion of the momentum distribution function using a perturbation parameter ϵ, expressed as $f = f^{(0)} + \epsilon f^{(1)} + \mathcal{O}(\epsilon^2)$, Enskog demonstrated Enskog 1917 that a first-order approximation of the Boltzmann equation yields the Navier-Stokes equations.

2.3 Acoustic Perturbation Equations

The generation and propagation of acoustic waves can be predicted using the acoustic perturbation equations. Here the APE-4 variant is used, which includes a source term for turbulence generated sound.

$$\frac{\partial \vec{u}'}{\partial t} + \nabla \left(\vec{\overline{u}} \cdot \vec{u}' + \frac{p'}{\overline{\rho}} \right) = \vec{q}_m \tag{7}$$

$$\frac{\partial p'}{\partial t} + \overline{c}_s^2 \nabla \cdot \left(\overline{\rho} \vec{u}' + \vec{\overline{u}} \frac{p'}{\overline{c}_s^2} \right) = 0 \quad , \tag{8}$$

Here, the time average is represented by $\overline{(\cdot)}$, and a perturbed quantity is defined as $(\cdot)' = (\cdot) - \overline{(\cdot)}$. For aerodynamically or turbulence induced noise at low Mach numbers, only the perturbed Lamb vector $\vec{L}' = (\vec{\omega} \times \vec{u})'$ is kept as an acoustic source, approximated by $\vec{q}_m \approx -\vec{L}'$. Further details are available in Ewert and Schröder 2003.

2.4 Ffowcs Williams and Hawkings Equations

The FW-H equation Williams and Hawkings 1969 is derived by precisely rearranging the Navier-Stokes equations — specifically, the conservation laws of mass, momentum, and

energy — into an inhomogeneous wave equation with a non-linear term on the right-hand side:

$$\left(\frac{\partial^2}{\partial t^2} - c_\infty^2 \frac{\partial^2}{\partial x_i^2}\right)[(\rho - \rho_\infty)H(f)] = \frac{\partial}{\partial t}[Q\delta(f)] - \frac{\partial}{\partial x_i}[F_i\delta(f)] + \frac{\partial^2}{\partial x_i \partial x_j}[T_{ij}H(f)] \tag{9}$$

$$Q = [\rho_\infty v_i + \rho(u_i - v_i)]\frac{\partial f}{\partial x_i} \quad \text{(Monopole term)},$$

$$F_i = [P_{ij} + \rho u_i(u_j - v_j)]\frac{\partial f}{\partial x_j} \quad \text{(Dipole term)},$$

$$T_{ij} = \rho u_i u_j + P_{ij} - c_\infty^2(\rho - \rho_\infty)\delta_{ij} \quad \text{(Quadrupole term)}\,.$$

The function f acts as a support function, taking a value of zero on the surface surrounding the volume of acoustic sources, a negative value within this volume, and a positive value outside it. The Heaviside step function, $H(\cdot)$, is unity when $f > 0$ and zero when $f < 0$. Here, $\mathbf{u}$ denotes the flow velocity, and $\mathbf{v}$ represents the velocity of the data surface f. The compressive stress tensor is given by $P_{ij} = (p - p_\infty)\delta_{ij} - \tau_{ij}$, where δ_{ij} is the Kronecker delta, and the viscous tensor τ_{ij} is typically neglected. Flow properties in the undisturbed far field are indicated by the subscript ∞. In the far field, the acoustic pressure is defined as $p' = c_\infty^2 \rho'$.

The first two terms on the right-hand side of the FW-H equation represent surface integrals, commonly known as the thickness source (or monopole) term and the loading source (or dipole) term. The final term, which corresponds to a volume integral, is the quadrupole source term. In low Mach number flows, this term is typically small compared to the other contributions. Additionally, this term is more difficult to compute and is often disregarded. The FW-H equation can be solved using Green's function of the wave equation, and the resulting solution can be expressed in either the time or frequency domain, as will be elaborated in the following section.

3 Numerical Methods

3.1 Finite-Volume Method for the Solution of the Navier-Stokes Equations

A finite-volume method is employed to discretize the non-dimensional conservation equations of mass, momentum, and energy, as outlined in eq. (1).

The discrete approximation is established for a Cartesian mesh incorporating immersed boundaries. A fully conservative cut-cell method is utilized for implementing boundary conditions at the domain boundaries Schneiders, Hartmann, et al. 2013. An explicit low-storage 5-stage Runge-Kutta scheme is employed to advance the solution in time, resulting in an overall method that is second-order accurate in both time and space. For further details on this approach, the reader is directed to Pogorelov, Meinke, and Schröder 2015. In the LES framework, turbulent structures are differentiated into a resolved part, which encompasses the dominant, large-scale, and most energetic eddies, and an unresolved part, which is addressed using a sub-grid scale model. The contribution from the sub-grid scales is modeled through the monotone integrated LES (MILES) approach Boris et al. 1992,

where the discretization error of the numerical scheme is leveraged to dissipate energy at the unresolved scales.

A level set method is employed to characterize the motion of embedded bodies. The level set function serves as a signed-distance function that partitions the domain into a solid region G^s and a fluid region G^f.

$$G^f(t) = \{x|\Phi(x,t) > 0\}\,, \quad \Gamma(t) = \{x|\Phi(x,t) = 0\}\,, \quad G^s(t) = \{x|\Phi(x,t) \leq 0\}. \tag{10}$$

The boundary of the body is represented by the zero level set contour Γ. To maintain the fidelity of the initial level set surface during the movement of the bodies, the kinematic motion level set technique as described by Günther, Meinke, and Schröder 2014 and Pogorelov, Schneiders, et al. 2018 is implemented. This approach involves interpolating the level set solution at each time step from the initial level set field established at the zeroth time step, which is reconstructed from high-resolution stereolithography (STL) data. Consequently, the error in the surface representation is solely attributed to the interpolation error and remains constant over time. This feature makes the method advantageous compared to other level set techniques, such as those relying on level set transport equations, where the accuracy of the geometric representation may degrade over time.

3.2 Cumulant Lattice Boltzmann Method

The discretization of eq. (6) results in the lattice Boltzmann equation

$$f_j(\vec{x} + \vec{c}_j\Delta t, t + \Delta t) = f_j^*(\vec{x}, t) = f_j(\vec{x}, t) + \Omega_j(f) + F_j\Delta t\,,$$

with the discrete particle velocity $\vec{c}_j = \vec{\xi}_j/\sqrt{3}$ in the discrete direction j. The asterisk $(*)$ denotes the post-collision state. In this study, the particle velocity space is represented using a three-dimensional Cartesian lattice with 27 discrete velocity directions, employing a D3Q27 model. Macroscopic flow quantities, such as density ρ and flow velocity $\vec{u}$, are derived from the moments of the particle probability distribution function (PPDF) that includes the external forcing term. The discrete integrals are expressed as

$$\rho(\vec{x}, t) = \sum_j f_j(\vec{x}, t) + \frac{\Delta t}{2}\sum_j F_j \quad \text{and} \quad \vec{u}(\vec{x}, t) = \frac{1}{\rho}\sum_j \vec{c}_j f_j(\vec{x}, t) + \frac{\Delta t}{2\rho}\sum_j \vec{c}_j F_j\,.$$

Here, the fluid velocity is redefined to incorporate the forcing term F_j, as derived in Guo, Zheng, and Shi 2002. The collision step, which involves evaluating the collision operator, can be implemented using either the Bhatnagar-Gross-Krook (BGK) operator Bhatnagar, Gross, and Krook 1954 or a cumulant collision operator Geier et al. 2015. The BGK operator is commonly utilized for low Reynolds number flows, while the cumulant collision operator has demonstrated greater stability and accuracy in modeling high Reynolds number flows, albeit at the cost of increased computational resources. The BGK operator is expressed as

$$\Omega_j = -\omega_{BGK}(f_j - f_j^{eq})\,,$$

where f_j^{eq} denotes the Maxwell equilibrium distribution function and ω_{BGK} the non-dimensional relaxation frequency

$$\omega_{BGK} = \frac{\Delta t c_s^2}{\nu_{eff} + \frac{1}{2}\Delta t c_s^2}\,. \tag{11}$$

The time step is denoted as Δt. The effective viscosity ν_{eff} encompasses the fluid viscosity, a turbulent viscosity computed using a Smagorinsky sub-grid scale model Hou et al. 1996, and an artificial viscosity that is applied solely in a sponge region near the boundaries of the domain to mitigate wave reflections. The equilibrium distribution for isothermal flow is approximated through a second-order expansion.

$$f_j^{eq} = w_j \rho \left(1 + \frac{\vec{c}_i \cdot \vec{u}}{c_s^2} + \frac{\vec{u}\ \vec{u} : (\vec{c}_j\ \vec{c}_j - c_s^2 \underline{\underline{I}})}{2 c_s^4 \phi} \right) , \tag{12}$$

where the weighting factors w_j are specified as follows: 8/27 for the rest, 2/27 for the six Cartesian directions, 1/54 for the twelve cubic edge-diagonal directions, and 1/216 for the eight cubic space-diagonal directions. To account for the presence of a porous medium, the porosity ϕ, defined as the ratio of void volume to total volume, is incorporated and derived from volume-averaging the lattice Boltzmann equation Guo and Zhao 2002. A suitable expression for the forcing term F_j is provided by

$$F_j = \left(1 - \frac{\omega}{2}\right) w_j \rho \left(\frac{\vec{c}_j \cdot \vec{F}}{c_s^2} + \frac{\vec{u}\ \vec{F} : (\vec{c}_j\ \vec{c}_j - c_s^2 \underline{\underline{I}})}{c_s^4 \phi} \right) .$$

The cumulant collision operator functions as a multiple relaxation time operator, which relaxes cumulants toward their equilibrium at distinct rates Geier et al. 2015. Cumulants are defined as the quantities obtained by Laplace-transforming the discrete particle probability distribution function (PPDF) from time-velocity space $\vec{\xi}$ to frequency-velocity space $\vec{\Xi} = \{\Xi, \Upsilon, Z\}$.

$$C_{\alpha\beta\gamma} = c^{-\alpha-\beta-\gamma} \frac{\partial^\alpha \partial^\beta \partial^\gamma}{\partial \Xi^\alpha \partial \Upsilon^\beta \partial Z^\gamma} \ln(F(\vec{\Xi})) \bigg|_{\vec{\Xi}=\vec{0}} , \text{with} \quad F(\vec{\Xi}) = \mathcal{L}\{f(\vec{\xi})\} = \int_{-\infty}^{\infty} f(\vec{\xi}) e^{-\vec{\Xi}\cdot\vec{\xi}} d\vec{\xi} .$$

The collision in cumulant space reads

$$C_\alpha^* = C_\alpha - \omega_\alpha (C_\alpha - C_\alpha^{eq}) ,$$

where C_α^{eq} denotes the Maxwellian equilibrium in cumulant space, and ω_α represents the associated relaxation frequency. Adhering to the terminology established by Geier et al. 2015, all relaxation rates are assigned a value of unity, except for ω_1. The propagation step and boundary conditions are executed following the transformation of the post-collision cumulants back into momentum space.

To minimize the number of grid points and, consequently, the computational effort, local grid refinement techniques are implemented. Specifically, the method proposed by Dupuis and Chopard Dupuis and Chopard 2003 is utilized, which employs different relaxation frequencies for various levels of refinement. To account for compressibility effects, an acoustic scaling approach is applied, ensuring that the computational time step is proportional to the grid spacing, such that $\Delta t \sim \Delta x$. From eq. (11), it follows that

$$\nu_{eff} = \Delta t c_s^2 \left(\frac{1}{\omega_{BGK}} - \frac{1}{2} \right) .$$

To maintain a consistent viscosity across the grid refinement interface, the relaxation frequency is adjusted in accordance with Δt. The no-slip boundary condition is enforced

using an interpolated bounce-back scheme Bouzidi, Firdaouss, and Lallemand 2001, which provides a second-order accurate representation of geometries with arbitrary shapes.

Simultaneously capturing the scales of turbulent flow around a realistic landing gear configuration, along with those present in the porous microstructure, is computationally demanding. To address this, volume averaging as illustrated in eq. (12) is employed, where the forcing term $\vec{F}$ represents a drag force exerted on the flow as it moves through a porous medium. This drag force is modeled using a Forchheimer-extended Darcy equation.

$$\vec{F} = \mathrm{C}_1 \vec{u} + \mathrm{C}_2 |\vec{u}| \vec{u} \,, \tag{13}$$

where C_1 and C_2 are model parameters that are specific to the porous material being analyzed and correspond to a particular range of operating conditions, such as bulk velocity. These parameters are determined through calibration against reference data derived from experimental measurements or simulations that resolve the microstructure.

3.3 Discontinuous Galerkin Spectral Element Method

The eqs. (7) and (8) are spatially discretized using a high-order nodal discontinuous Galerkin spectral element method (DGSEM). This section provides only a brief outline of the DGSEM; for more comprehensive details, the reader is referred to Kopriva, Woodruff, and Hussaini 2000; Kopriva, Woodruff, and Hussaini 2002; Hindenlang et al. 2012, or specifically to Schlottke-Lakemper, Yu, et al. 2017 for the particular implementation utilized within the m-AIA simulation framework.

The solution procedure in d dimensions involves several key steps. Initially, the equations within each grid cell are mapped from physical space, denoted as $\vec{x}$, to reference space $\vec{\xi} \in [-1, 1]^d$ through the mapping $\vec{x}(\vec{\xi})$. Next, these equations are multiplied by test functions and integrated over the reference element E. Following this, integration by parts is applied to derive the weak formulation.

In each element, the solution space is approximated using a tensor product ansatz of piecewise polynomials with a maximum degree of N, represented as the function space $\mathbb{P}^N(E)$. A complete set of basis functions is constructed using Lagrange interpolating polynomials, denoted as $l_i(\xi) i = 0^N$, which are defined by a specific set of interpolation nodes $\xi_i i = 0^N$. This results in the condition $l_i(\xi_j) = \delta_{ij}$. Consequently, the solution vector can be expressed as

$$\vec{U}(\vec{\xi}, t) \approx \vec{U}_h(\vec{\xi}, t) = \sum_{i,j=0}^{N} \hat{\vec{U}}_{ij}(t) \psi_{ij}(\vec{\xi}) \quad \text{with} \quad \psi_{ij}(\vec{\xi}) = l_i(\xi) l_j(\eta) \tag{14}$$

For the case of two dimensions, i.e., $d = 2$, the nodal degrees of freedom are denoted as $\hat{\vec{U}}_{ij}$. Both the fluxes and the sources are approximated using the same nodal expansion as indicated in eq. (14). Given the discontinuity of the solution space at the boundaries of the elements ∂E, the surface flux is replaced by a numerical flux, specifically the local Lax-Friedrichs flux.

Following the Galerkin ansatz, the test functions $\vec{\varphi}$ are also selected from $\mathbb{P}^N(E)$, with the particular choice being $\vec{\varphi} = \vec{\psi}$. The space integrals are computed using a numerical quadrature rule. A collocation-type discretization is employed, utilizing integration nodes

$\xi_i i = 0^N$ and weights $wi = 0^N$, which results in an orthogonal approximation space and a diagonal discrete mass matrix because of the condition $l_i(\xi_j) = \delta_{ij}$. For this purpose, either Legendre-Gauss nodes, which provide an integration precision of $2N + 1$, or Legendre-Gauss-Lobatto nodes, which achieve an integration precision of $2N - 1$, can be used. The resulting semi-discrete ordinary differential equation is then integrated over time using a suitable time integration scheme.

In the work presented in Gassner and Kopriva 2011, it was demonstrated that for the majority of combinations of polynomial order and accuracy bounds, the Gauss discontinuous Galerkin spectral element method (DGSEM) outperforms the Gauss-Lobatto DGSEM in terms of the required points per wavelength (PPW). Consequently, the Gauss DGSEM is selected as the preferred method for the cases in this paper. To achieve an overall fourth-order spatial discretization, third-order basis functions will be employed, unless stated otherwise.

3.3.1 Immersed Boundary Formulation of Acoustic Perturbation Equations

Since the CAA solver utilizes a Cartesian mesh, all curved boundaries within the domain are immersed in the computational mesh. The following sections will discuss the accurate, efficient, and robust numerical formulations for handling immersed boundaries in the high-order DGSEM Kopriva, Woodruff, and Hussaini 2000; Kopriva, Woodruff, and Hussaini 2002; Schlottke-Lakemper, Yu, et al. 2017.

To model the acoustic scattering effects from solid surfaces, the approach involves treating solid bodies as permeable media, approaching the limit of vanishing porosity $\phi \to 0$ and permeability $\kappa \to 0$. From these assumptions, physically motivated model terms can be derived, which are incorporated into the acoustic perturbation equations (APE). In the case of a solid, non-permeable body, the formulation of the porous model terms can be modified to create a robust discrete system.

The approach described below closely aligns with the principles of the Brinkman Penalization Method (BPM) and the Impedance Mismatch Method (IMM) Chung and Morris 1998; Laik and Morris 2000. The BPM, initially developed for incompressible flows with rigorous error estimates Angot, Bruneau, and Fabrie 1999, has been adapted to the compressible framework in Liu and Vasilyev 2007 and has also been applied to problems involving acoustic scattering, as demonstrated in Bae and Moon 2012.

The core idea of the IMM is to represent a solid body as a region characterized by a higher impedance, defined as $Z = \rho c_s$. According to acoustic theory, this increased impedance will naturally reflect waves that encounter this region. For numerical convenience, Chung Chung and Morris 1998 addressed an auxiliary problem with $Z \propto 1/\rho$, where the impedance is adjusted by the mean density ratio while maintaining a constant speed of sound to preserve the same Courant-Friedrichs-Lewy (CFL) condition.

In the compressible BPM formulation introduced by Liu Liu and Vasilyev 2007, in addition to penalizing the momentum and energy equations, porosity is incorporated into the continuity equation typical of porous media, effectively simulating a high-impedance region that parallels the concepts employed in the IMM.

After evaluating various options for accuracy, robustness, and implementation simplicity, the following set of equations is proposed, applicable throughout the entire CAA domain.

$$\frac{\partial \vec{u}'}{\partial t} + \nabla \left(\vec{\overline{u}} \cdot \vec{u}' + \overline{c}_s^2 \frac{\rho_s'}{\overline{\rho}} \right) + \underline{\underline{R}}\, \vec{u}' = \vec{q}_m \tag{15}$$

$$\frac{\partial \rho_s'}{\partial t} + \frac{1}{\phi} \nabla \cdot \left(\phi \overline{\rho} \vec{u}' + \phi \vec{\overline{u}} \rho_s' \right) = 0. \tag{16}$$

The equations presented can be interpreted as a formal derivation obtained by volume averaging eqs. (7) and (8) over a porous medium characterized by porosity ϕ. In order to utilize a conservative numerical scheme, we introduce the equivalent density fluctuation $\rho_s' = p'/\overline{c}_s^2$, which corresponds to the pressure fluctuation within an isentropic acoustic medium. Additionally, given that ϕ remains constant over time, we consolidate the porosity to create a superficial isentropic density perturbation. Thus, eqs. (15) and (16) are solved for the vector $(\vec{u}', \phi\rho_s')^T$. This approach eliminates the necessity for specialized numerical treatment at the porosity interface and facilitates a straightforward spatial discretization. Furthermore, the quantity $\underline{\underline{R}} = \frac{1}{\kappa}\vec{n} \otimes \vec{n}$ represents the 'anisotropic' permeability tensor, where $\vec{n}$ is the unit normal vector of the solid body. This tensor was introduced in Bae and Moon 2012 to enforce the slip boundary condition in compliance with the first-order APE system.

Note that it does not contradict acoustic theory that, similar to Chung and Morris 1998, in the present method the effective density is smaller in the solid body region. This occurs because, in the APE, a portion of the linearized terms is shifted to the right-hand side source vector, which inverts the impact of density variations on the wave operator. The present IB treatment effectively reduces to replacing the density with an effective density $\overline{\rho}_{\text{eff}} = \phi\overline{\rho}$ during the initialization of the mean field and applying a penalty term. Indeed, two contributions can be identified. The assumption of uniform mean density across the fluid-solid interface yields the theoretical reflection coefficient for plane waves

$$R(\omega, \phi, \kappa) = \frac{\tilde{Z}_{\text{solid}} - \phi}{\tilde{Z}_{\text{solid}} + \phi} \in \mathbb{C} \quad \text{with} \quad \tilde{Z}_{\text{solid}} = \sqrt{1 - \frac{i}{\omega\kappa}}, \tag{17}$$

where $i = \sqrt{-1}$, ω represents the angular frequency, and $\tilde{Z}_{\text{solid}}$ denotes the relative impedance of the solid region. It is important to note that a frequency-independent formulation can be established that eliminates phase error $\Im(R)$ by incorporating a pressure relaxation term and adjusting the flux Jacobians. Nonetheless, empirical tests revealed that this method lacks numerical robustness, and the resulting poor frequency response for linear acoustics is unlikely to significantly impact the acoustic field. Numerical trials suggest that using $\kappa \propto \mathcal{O}(10^{-2})$ serves as a good compromise between uncertainties regarding the precise boundary interface location when $\kappa \to \infty$ and the behavior of wave reflections.

3.3.2 Time Integration and Discussion of Stability

In the fluid region, where $\phi = 1$ and $\kappa \to 0$, the semi-discretized equations are integrated in time using an explicit five-stage fourth-order low-storage Runge-Kutta (ERK) method Carpenter and Kennedy 1994. However, the stability of the system as $\phi \to 0$ and $\kappa \to 0$ is constrained by two numerical issues. The first issue arises from the immersed

boundary (IB) treatment, which alters the flux vector into a rational function, leading to inexact quadrature. Various stabilization strategies for mitigating this aliasing error have been proposed in the literature, such as solving a split form of the equations, employing modal filtering to increase numerical dissipation, or implementing overintegration techniques for the affected terms. Unfortunately, none of these methods have proven to ensure unconditional stability with Gauss DGSEM, as they do not yield positive eigenvalues for the space operator in the current context. A remedy for this problem is to switch to Gauss-Lobatto DGSEM in a thin layer surrounding the solid bodies, i.e., for $\phi < 1$, which has been found to provide an unconditionally stable semi-discrete system while allowing Gauss DGSEM to be used elsewhere. Gauss-Lobatto DGSEM incorporates the boundary points and adheres to the summation-by-parts (SBP) property, the discrete equivalent of integration-by-parts. Coupled with a diagonal mass matrix, resulting from the collocation approach where $l_i(\xi_j) = \delta_{ij}$, this facilitates the application of energy and entropy proofs to the discrete scheme. Lower porosity values ϕ lead to a space operator with larger spectral radii, imposing a stricter time step constraint for explicit integration methods. To ensure the eigenvalue spectrum remains within the linear stability envelope of the ERK method, a porosity of $\phi = 1/15$ is selected for the subsequent computations.

The second limitation stems from the stiffness introduced by the penalty terms. In this context, the system is decomposed into a linear stiff component and the remaining part, allowing the ERK method to be combined with a sixth-stage formally second-order explicit, singly-diagonally implicit Runge-Kutta (ESDIRK) method, also implemented in a low-storage format, resulting in an implicit-explicit Runge-Kutta (IMEX-RK) scheme. The low-storage algorithm and the corresponding coefficients for the ESDIRK method are presented in table 1. For the steady permeability tensor $\underline{\underline{R}}$, which contains only local geometric information, this approach necessitates a single inversion of a local coefficient matrix $\underline{\underline{I}} - b\Delta t\underline{\underline{R}}$, which is precomputed during initialization and reused in RK sub-stages 2 through 6.

$$
\begin{aligned}
\vec{Q}^{(0)} &= (\vec{u}'^{,n}, \rho_s'^{,n})^T \\
\mathrm{d}\vec{Q}^{(0)} &= \underline{\underline{R}}\,\vec{Q}^{n} \\
\left.\begin{aligned}
\vec{Q}^{(i-1)} &\xrightarrow{\text{ERK}} \vec{Q}^{(i^*)} \\
\mathrm{d}\vec{Q}^{(i)} &= a_i \mathrm{d}\vec{Q}^{(i-1)} + \underline{\underline{R}}\,\vec{Q}^{(i)} \\
\vec{Q}^{(i)} &= \vec{Q}^{(i^*)} + b\Delta t \mathrm{d}\vec{Q}^{(i)}
\end{aligned}\right\} &\begin{aligned} &\text{i=1,}\ldots\text{, 5} \\ &t^i = t^n + c_i\Delta t \end{aligned} \\
\vec{Q}^{n+1} &= \vec{Q}^{(5)}
\end{aligned}
$$

a_i	c_i
0.0841951687384	0.149659021999
0.552622613121	0.3704009573642
0.515614896786	0.6222557631344
0.786125130248	0.9582821306747
-0.286641512481	1.0

Table 1: The implementation of the six-stage stiffly-stable ESDIRK scheme follows a $2N$-storage approach. In this configuration, the intermediate time levels for both the ERK and ESDIRK methods are held equal. The coefficients utilized in this scheme are rounded to twelve significant digits, with the coefficient b specified as 0.138036975551.

3.4 Ffowcs Williams and Hawkings Method

Farassat has derived a solution to the FW-H equation in time domain. Formulation 1A Brentner and Farassat 1998 is extensively utilized for predicting noise generated by rotors and propellers. This formulation presumes a moving acoustic source immersed within a stationary ambient fluid, with noise measurements taken by a stationary observer located in the far field. The free-space Green's function is expressed as $G = \frac{\delta(g)}{r}$, where $g = t - \tau - \frac{r}{c_\infty}$ and $r = |\mathbf{x} - \mathbf{y}|$. Here, t and τ denote the times of the observer and source, respectively, while $\mathbf{x}$ and $\mathbf{y}$ represent the coordinates of the observer and source, respectively. The acoustic pressure p' can be separated into thickness and loading noise components.

$$p'(\mathbf{x}, t) = p'_T(\mathbf{x}, t) + p'_L(\mathbf{x}, t) \tag{18}$$

with

$$4\pi p'_T(\mathbf{x}, t) = \int_{f=0} \left[\frac{\rho_\infty (\dot{U}_n + U_{\dot{n}})}{r(1 - M_r)^2} + \frac{\rho_\infty U_n (r\dot{M}_r + c_\infty (M_r - M^2))}{r^2 (1 - M_r)^3} \right]_{ret} dA \tag{19}$$

$$4\pi p'_L(\mathbf{x}, t) = \int_{f=0} \left[\frac{\dot{L}_r}{c_\infty r(1 - M_r)^2} + \frac{L_r - L_M}{r^2(1 - M_r)^2} + \frac{L_r (r\dot{M}_r + c_\infty (M_r - M^2))}{c_\infty r^2 (1 - M_r)^3} \right]_{ret} dA \tag{20}$$

Here, the source terms U_n and L_i are defined as

$$U_n = [v_i + \rho/\rho_\infty (u_i - v_i)]\hat{n}_i \tag{21}$$

$$L_i = [(p - p_\infty)\delta_{ij} + \rho u_i (u_j - v_j)]\hat{n}_j \tag{22}$$

where $\hat{n}_i = \partial f / \partial x_i$ denotes the unit outward surface normal vector. $\mathbf{M}$ is the Mach number vector of the source surface, with component $M_i = v_i / c_\infty$. The unit vector in the radiation direction is expressed as $\hat{r}_i = (x_i - y_i)/r$. The superscript $(\cdot)$ represents the derivative with respect to the source time $\partial / \partial \tau$. The subscript $[...]ret$ denotes the evaluation of the integrand at the time of emission, with the retarded time $\tau = t - r/c_\infty$.

In wind tunnel experiments and computational fluid dynamics simulations, domains are typically defined using an Eulerian coordinate system, which assumes fixed sound sources and observers in a uniform incoming flow. To apply Formulation 1A, which is derived for quiescent ambient flow, a coordinate transformation is necessary in these scenarios. For instance, consider a simulation setup with a mean incoming flow velocity in the $+x_1$ direction, specifically $\mathbf{U}_\infty = (U_{\infty,1}, 0, 0)$. This setup is equivalent to having a control volume moving at a velocity of $V = -U_\infty$ within a quiescent fluid, with the sources and observers fixed relative to this frame of reference. Consequently, the sound source measured in the relative frame will first be transformed to the absolute frame before being applied to Formulation 1A.

$$[u_i]_{abs} = [u_i]_{rel} + V, \qquad [v_i]_{abs} = [v_i]_{rel} + V. \tag{23}$$

Additionally, to account for the influence of uniform flow motion on the retarded time, the geometric distance r in Formulation 1A must be substituted with the effective acoustic distance R Brès, Pérot, and Freed 2010.

The FW-H equation is more efficiently solved in the frequency domain compared to the time domain. Following the work of Lockard 2000, we apply a Galilean transformation along with a Fourier transformation to the equation, assuming that the surface defined by $f = 0$ moves in a straight line at a constant speed. The solution to the frequency-domain FW-H equation for subsonic flow is given by:

$$H(f)c_\infty^2\rho'(\mathbf{y},\omega) = -\oint_{f=0} i\omega Q(\boldsymbol{\xi},\omega)G(\mathbf{y};\boldsymbol{\xi})dA - \oint_{f=0} L_i(\boldsymbol{\xi},\omega)\frac{\partial G(\mathbf{y};\boldsymbol{\xi})}{\partial \xi_i}dA - \int_{f>0} T_{ij}(\boldsymbol{\xi},\omega)H(f)\frac{\partial^2 G(\mathbf{y};\boldsymbol{\xi})}{\partial \xi_i \partial \xi_j}d\boldsymbol{\xi}, \tag{24}$$

with the angular frequency ω and the Green's function $G(\mathbf{y};\boldsymbol{\xi})$. The coordinates for the three-dimensional source and observer are represented by $\boldsymbol{\xi}$ and $\mathbf{y}$, respectively.

3.5 Coupling Algorithm for the CFD/CAA Method

In the direct-hybrid method, a joint hierarchical Cartesian grid is utilized for both the CFD and CAA solvers Schlottke-Lakemper, Yu, et al. 2017. Mesh refinement occurs during the grid generation process, tailored individually to meet the constraints of each solver. All cells are labeled according to their assignments to the respective solvers. These cells are organized within an octree data structure that maintains parent, child, and neighbor relationships Hartmann, Meinke, and Schröder 2008. Consequently, each coarse partition cell serves as the root cell of a subtree encompassing the entire grid.

The computational grid is partitioned at this coarse level, where a Hilbert space-filling curve (SFC) is employed to achieve a one-dimensional ordering of all partition cells. A computational workload is assigned to each cell of the joint grid based on its utilization by one or both solvers. By traversing the subtrees of the grid, the total workload for each coarse partition cell is calculated. Domain decomposition is then performed by splitting the Hilbert curve to create partitions of equal size in relation to the workload. Each partition, which consists of a spatially compact set of partition cells along with their corresponding subtrees, is assigned to a dedicated parallel process.

The partitioning strategy, which operates on the joint Cartesian mesh, enables efficient coupling between the solvers. This is because all CFD and CAA cells located within the same physical volume of the three-dimensional domain are assigned to the same process, allowing for in-memory exchange of the data that includes the acoustic source terms. Spatial interpolation from the CFD to the CAA solution representation is achieved through local Galerkin projection Schlottke-Lakemper, Niemöller, et al. 2019, which accommodates arbitrary spatial mappings while relying solely on locally available data. The locality property of the chosen SFC inherently ensures intra-process spatial compactness of the cells, generating compact surfaces of the subdomains and thus reducing communication overhead.

In this study, the time step for the FV based CFD simulation is set equal to the time step used in the DG based CAA simulation. Consequently, temporal interpolation

of source term data, such as through quadratic interpolation Koh, Schröder, and Meinke 2010, is unnecessary. The parallel coupled algorithm alternates between advancing the Runge-Kutta time integration stages of both solvers. For a more detailed explanation of the coupling approach, refer to Schlottke-Lakemper, Yu, et al. 2017.

For the coupling of the LB method with the DG approach, the procedure varies slightly. First, the solvers advance the solution by a full time step alternately, as the LB method does not utilize a multi-stage Runge-Kutta time integration scheme, which makes it more challenging to hide the communication of the CAA solver behind the CFD computation. Second, the time step for the CAA solver is chosen to align with the time step of a specific LB refinement level. As a result, the time steps for the LB method on coarser levels than this specific grid level are multiples of the CAA time step. In this study, the specific refinement level is set to the finest level in the LB method, and the acoustic source terms calculated by the LB method on the coarser levels remain constant for the DG method until a matching time level for the corresponding cells is attained.

4 Use Cases

4.1 Laminar Flow around a Circular Cylinder

The first use case illustrates an application of the various numerical methods described in section 3 for a laminar unsteady flow, i.e., the flow around a circular cylinder at low Reynolds number. The main purpose is a validation of all methods. The use case follows the DNS setups by Inoue and Hatakeyama 2002, illustrated in fig. 1. The cylinder has a diameter of $D = 1$. The inflow Mach number is $M = 0.2$, and the Reynolds number based on the cylinder diameter is $Re = 150$ or 200.

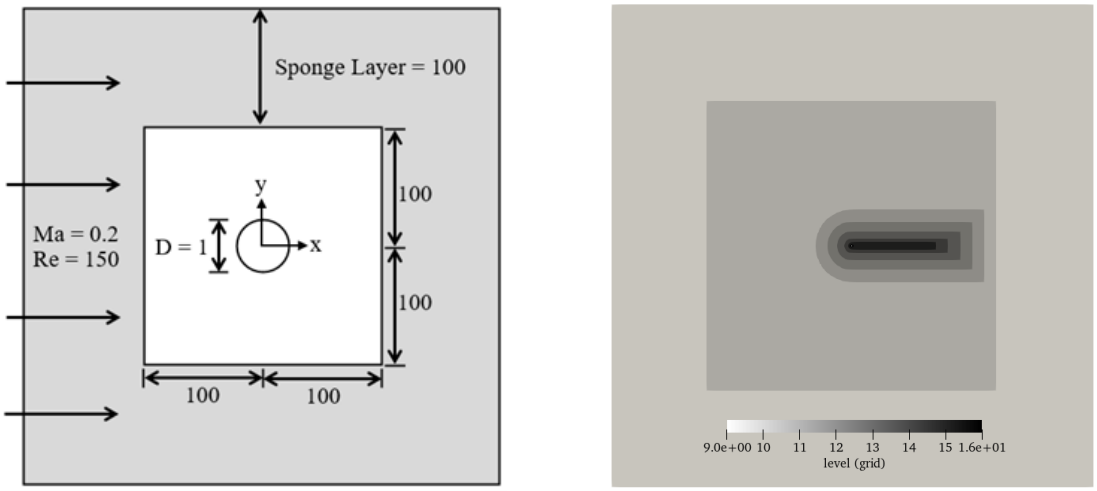

Figure 1: Computational domain (left) and local mesh refinement (right)

The two-dimensional computational domain has a streamwise and cross-streamwise length of $400D$. An unstructured Cartesian mesh with 5.4 million cells has been generated. It employs isotropic local mesh refinement to improve the resolution in the boundary layers

and vortex-shedding region, resulting in the minimum $\Delta x/D = 0.006$ and maximum $\Delta x/D = 0.781$.

As for the boundary conditions, the non-slip adiabatic boundary condition has been used for solid wall surfaces. Subsonic inlet and outlet have been implemented for the far-field boundary. An acoustic sponge layer with a thickness of $100D$ is applied to the far-field boundary to absorb pressure reflections.

The finite volume (FV) solver and the Lattice Boltzmann (LB) solver share the same Cartesian mesh and the same temporal resolution Δt for the simulations. The simulation is first carried out for an acoustic time of $tc/D = 1000$ until the vortex-shedding pattern is fully developed. Then postprocessing modules are activated to record the near-field flow field signal on a FW-H surface for another 50 vortex-shedding periods. The location of the permeable FW-H surface is shown in fig. 2. The surface is $5D$ away from the cylinder center, extended to $30D$ downstream, with a spatial resolution of $0.05D$ and a sampling rate of $St = 355$.

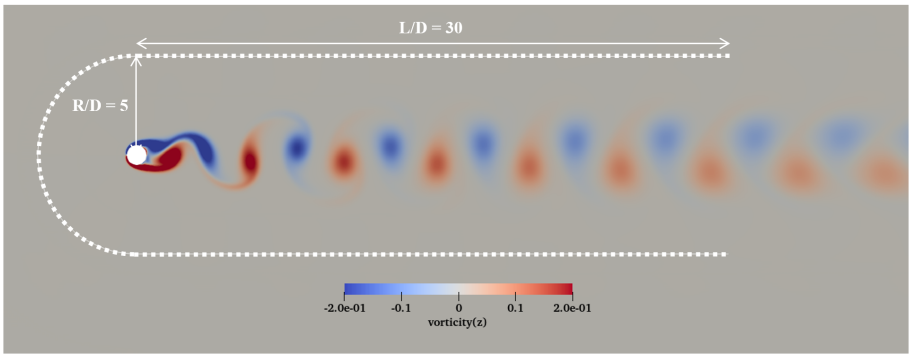

Figure 2: Contours of the vorticity and location of the permeable FW-H surface defined by the white dotted line.

The predicted instantaneous pressure field by the FV solver is plotted in fig. 3. A dipole-shaped noise source can be observed from the flow field due to the periodic vortex shedding of the cylinder. The white dotted line in the plot represents the observers from the near field $r/D = 1$ to the far field $r/D = 100$ for further comparison.

Next, the numerical results are compared with the reference DNS results by Inoue and Hatakeyama 2002, in fig. 4, including the direct simulation predictions of the FV and LB solver, and results of the hybrid approaches of the FV + FW-H and LB + FW-H. Figure 4(a) plots the numerical results from the fine Cartesian mesh with minimum $\Delta x/D = 0.006$. It can be found that the results of all prediction methods agree well with the reference solution. In comparison, the predicted results from a coarse mesh with minimum $\Delta x/D = 0.048$ are plotted in fig. 4(b). It can be seen that for an insufficient near-wall mesh resolution, the FV solver tends to overpredict the noise source, resulting in the overestimation of the FV + FW-H results. On the contrary, the LB solver underestimates the noise source, leading to an underestimation of the LB + FW-H predictions.

The performance of the FV and LB CFD solvers implemented in m-AIA, are compared in fig. 5(left). It can be seen that the cummulant based LB method is approximately 4 times faster per time step compared to the FV method. Note that this factor heavily depends on the use case, HPC hardware and also the current implementation. If the FV and

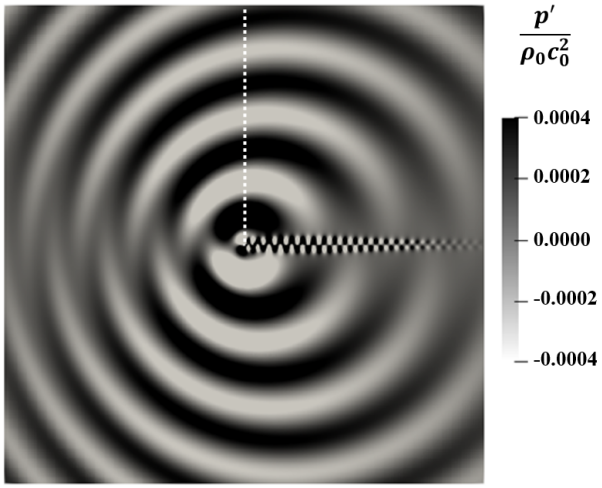

Figure 3: Instantaneous pressure field predicted by the FV solver on the fine Cartesian mesh

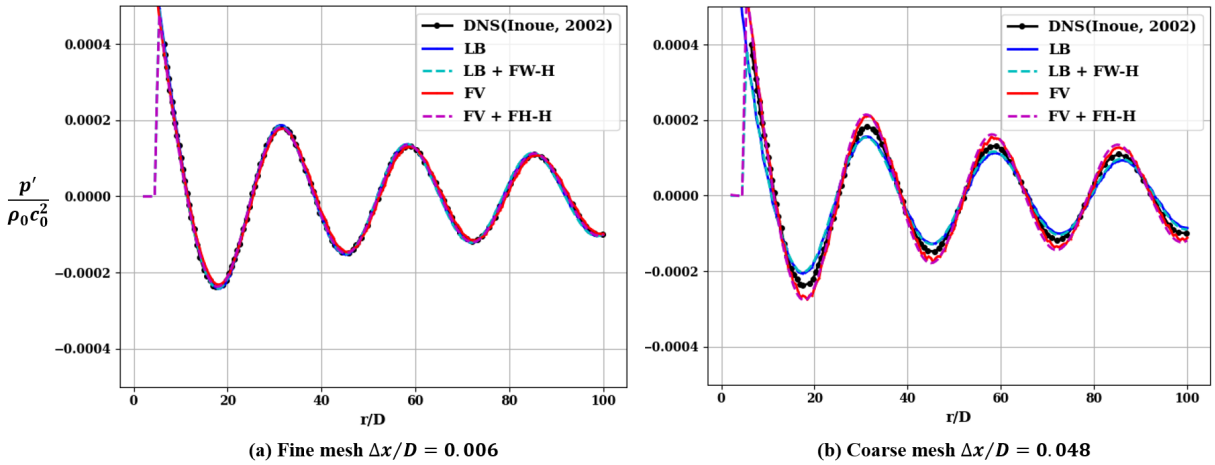

Figure 4: Comparison of the predicted pressure signal on (a) fine mesh and (b) coarse mesh

LB method are directly coupled with the CAA method, the advantage of the LB method is clearly reduced as shown in fig. 5(right), since a perfect interleaving of the computational work in the LB and DG solvers is not possible, see Gondrum, Satcunanathan, et al. 2023 for more details. Again, this result depends on the hardware and implementation of the solvers and also the used coupling strategy.

Figure 6 shows the predicted perturbed lamb vector field, which serves as the input for the APE system, and the pressure distribution along a line. The results of both direct-hybrid methods for the laminar flow around the cylinder at M=0.3 and Re=200 agree fairly well with the DNS results of Ewert and Schröder 2003.

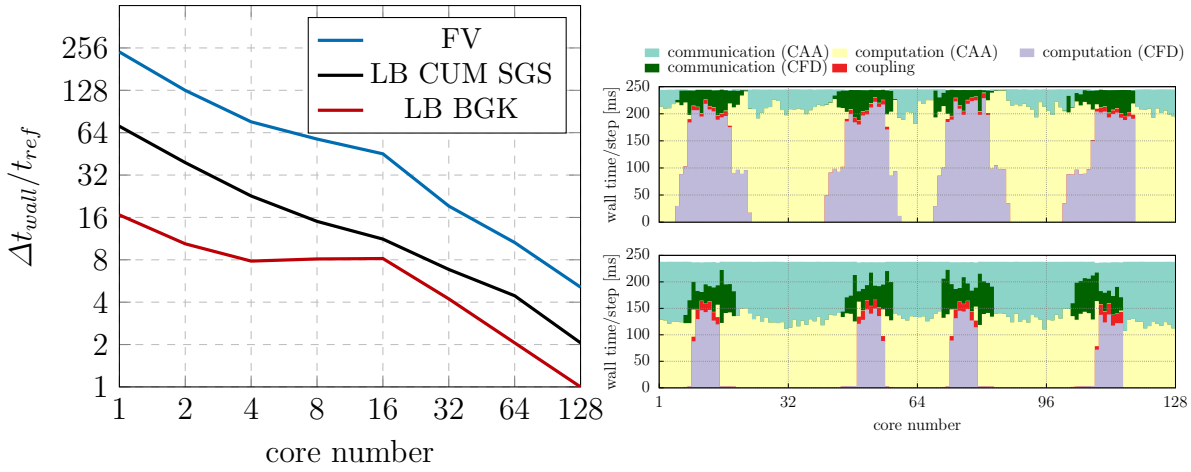

Figure 5: Performance measurements performed on two *AMD EPYC 7742* CPUs with 64 cores each. Left: Comparison of the wall time per time step between the presented FV and LB methods implemented in m-AIA for an isotropic refined periodic three-dimensional domain with 64^3 grid points. For the LB method, the BGK and the cumulant collision kernel including a Smagorinsky SGS model are considered. t_{ref} is the wall time of the LB BGK executed on 128 CPU cores. Right: Load distribution for two direct-hybrid simulations of a co-rotating vortex pair, see Gondrum, Satcunanathan, et al. 2023. Shown are the shares of the computing and communication time for the coupled FV/DG and LB/DG solvers versus the MPI processes executed on the individual CPU cores. Top: FV/DG, bottom: LB/DG.

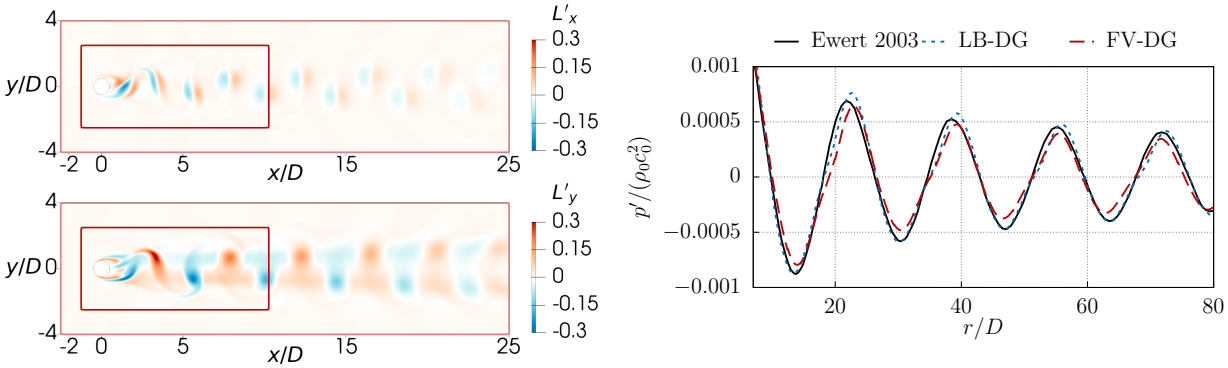

Figure 6: Left: Contours of the x- and y-component of the perturbed Lamb vector $\vec{L}'$ showing the source term region by red lines (–). From the inner to the outer red box, the acoustic sources are gradually reduced to zero. Right: Instantaneous pressure distributions along the line $x = 0$ for the two direct-hybrid methods as well as for the DNS reference solution by Ewert and Schröder 2003.

4.2 Landing Gear Noise

In this section, a typical example for airframe noise is investigated to illustrate an application of the LB method combined with the FW-H approach. The results were obtained in the EU project INVENTOR Gondrum, Meinke, et al. 2024.

4.2.1 Geometry and Computational Setup

A two-wheel nose landing gear with a wheel diameter of $D = 150$ mm, approximately corresponding to a 1:7 scale of a real nose landing gear (LG), is the subject of the present use case. The landing gear features a simplified geometry, including brakes, a torque link, and a detachable fairing, as illustrated in fig. 7. The fairing is positioned $0.37D$ in front of the strut, which has a height of $1.8D$ and a width of $0.36D$, covering the torque link, parts of the brakes, and the lower strut.

The landing gear is mounted on a flat plate and is investigated at a wheel-based Reynolds number of $Re_D \approx 346,000$ and a freestream Mach number of $M_\infty \approx 0.1$. The geometric parameters and flow conditions are summarized in table 2.

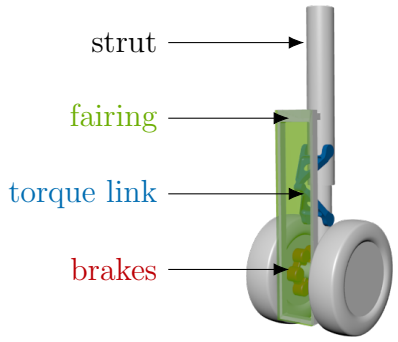

Figure 7: Landing gear featuring brakes (red), torque link (blue), and fairing (green). The fairing is replaced by different kind of materials. Each feature including the fairings' holder is removable.

Wheel diameter D	150 mm
Upper strut diameter	0.24 D
Distance axle-wall	2.33 D
Outer wheel base	0.95 D
Fairing to strut distance	0.37 D
Fairing height	1.8 D
Fairing width	0.36 D
Mach number M_∞	0.10198
Wheel Reynolds number Re_D	346,306
Upper strut Reynolds number Re_S	83,113

Table 2: LG geometry and flow parameters.

Three different kinds of fairings are investigated: a solid fairing and two porous fairings. The porous material is constructed by clustering multiple units of the diamond lattice structure depicted in fig. 8. Each of these cells fits within a cubic box with an edge length of l. The structure consists of struts with a diameter of $d_s \approx 0.18l$ that are oriented at an angle of 60° with respect to each other, resulting in a pore diameter of $d_p \approx 0.16l$ and a porosity of $\phi = 61.7\%$.

Two fairings with different cell sizes and fairing thicknesses are examined. Due to the large discrepancy in length scales between the flow structures inside the porous material and those around the landing gear, the material is modeled using volume-averaging techniques as described in section 3.2. The model parameters are obtained through calibration against pressure drop results from numerical simulations as well as experimental data from Delft University of Technology, and are summarized in table 3.

The computational domain has a total extent of $130D \times 65D \times 32.5D$. The physical relevant part of the domain excluding a sponge area, where artificial viscosity is introduced to damp waves reflected back into the domain, is $80D \times 40D \times 20D$. The domain is discretized with a Cartesian grid, where the grid spacing on a refinement level r is given by $\Delta x_r = L/2^r$. Here, Δx_0 represents the length of a cubic bounding box of the computational domain with a length of $L = 130D$. The grid is refined at refinement

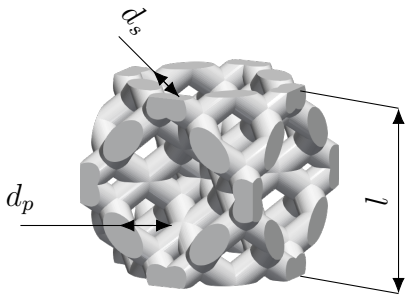

Figure 8: Unit cell of the diamond lattice structure.

Abbreviation	*DL2.5*	*DL6.4*
Size of unit cell l	2.5 mm	6.4 mm
Fairing thickness L_f	2 l	1 l
Porosity ϕ	61.7 %	
Pore diameter d_p	0.1888 l	
Strut diameter d_s	0.1648 l	
C_1 [1/s]	-4,431	-833
C_2 [1/m]	-15,320	-4,060

Table 3: Geometry of the diamond lattice structure and modeling parameters for the two porous fairings.

patches as shown in fig. 9 starting from a refinement level of $r_{min} = 9$. At the LG's surface a boundary refinement within a thickness of $0.02D$ on the maximum refinement level corresponding to a grid resolution of $\Delta x_{max} = 1/1008D$ is applied. The transition to the next patch refinement level is created with at least 10 layers of cells, see fig. 10. This yield a total number of 705-850 million grid points and a computational time step of $\Delta t = 2.5 \cdot 10^{-7} s$. The LG surface is represented by a no-slip interpolated bounce-back boundary condition, whereas the mounting plate is considered simplified as a slip wall such that the boundary layer on the mounting plate is not resolved. The in- and outflow are described by non-reflecting characteristic boundary conditions extending the work of Izquierdeo and Fueyo Izquierdo and Fueyo 2008 into three space dimensions. By solving the local one-dimensional inviscid (LODI) equations, which resemble the Euler equations without transverse derivative terms, waves being reflected back into the domain are mitigated. The determined macroscopic state is set through the corresponding equilibrium state. The remaining boundaries are defined by pressure equilibrium boundary conditions, i.e., the velocity is extrapolated from the interior domain, while the pressure/density is prescribed to be at ambient conditions. The presented setup is validated in Gondrum, Niemöller, et al. 2022 against experimental measurements provided by Delft University of Technology.

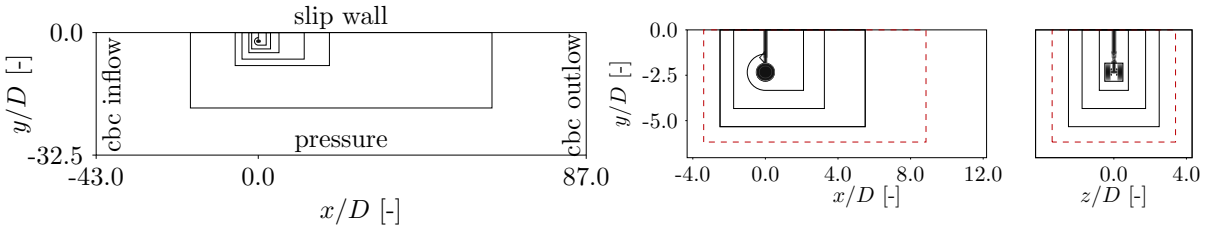

Figure 9: Numerical setup of the CFD/CAA flow simulation. 2D slices showing the dimension of the refinement patches in black lines (–). On the left, a slice of the complete domain starting with a refinement level of 9 is shown. The two figures on the right show details starting with a refinement level of 12. In addition, the location of the FW-H permeable surface is represented by a dashed red line (-·),

To predict the acoustic far field by the FW-H method, time resolved flow field data is sampled during the LB solver run on a FW-H surface. The surface position is depicted

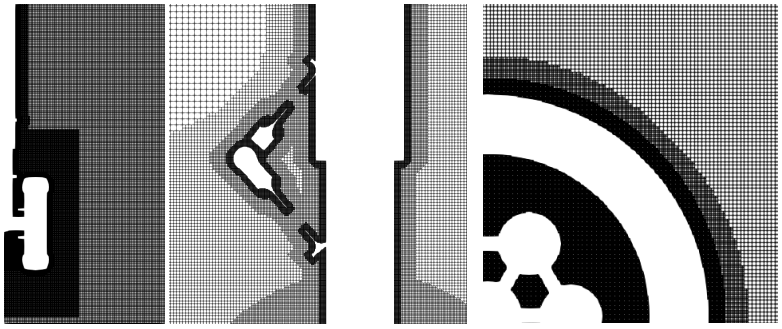

Figure 10: Details of the grid refinement around the wheel, torque link, and brakes for the grid. Only every second grid point is shown.

Δx_{fwh}	0.03 D
noElements	1,389,606
$\Delta t_{sampling}$	1 / 124kHz
$T_{sampling}$	27 / 0.2kHz
noSampling	16,384

Table 4: Properties of the surface grid and the temporal sampling of the FW-H method's input data.

in fig. 9. It is discretized using a uniform right-angled trianglular grid with a maximum edge length of the underlying CFD grid of $\Delta x_{fwh} = 0.03D$. Thus, an acoustic wave with a frequency in the experiment of $9kHz$ is resolved with more than 8 grid points. The data is sampled with a frequency of $124kHz$ over a period of $T_{sampling} = 27/(0.2kHz)$. Table 4 summarizes the sampling settings and the details of the FW-H surface grid.

4.2.2 Turbulent Flow Field around the Landing Gear

In this section, the influence of the different fairings on the turbulent flow field is discussed and the numerical approach of the treatment of the porous fairings as described in section 3.2 is verified. Therefore, comparisons with experimental data of *Delft University of Technology* (TUD) are provided. The corresponding experimental setup is explained in our previous study Gondrum, Niemöller, et al. 2022.

The instantaneous velocity field computed for the two reference configurations, i.e., the baseline LG and the baseline LG with a solid fairing, is visualized on isovolumes of the Q-criterion Hunt, Wray, and Moin 1988 in fig. 11. Both velocity fields are characterized by detached flows resulting in a turbulent wake. Due to the shielding properties of the solid fairing, vortical structures forming at the torque link interacting downstream with the strut as well as the highly turbulent flow in the region of the brakes are mitigated. Therefore, at the top of the fairing and in front of the strut an additional vortex forms. Also, the flow around the wheel is influenced by the lateral flow acceleration such that the separations at the outside of the wheels are amplified. In fig. 12, the pressure distribution over the left wheel for the four configuration is plotted. It fairly reproduces experimental measurements. Deviation from the experiment are observable for the baseline configuration. At this point it must be noted that in the experiment a zig-zag transition strips are added on the wheel at an angle of $\theta = \pm 60°$, but left unconsidered in the numerical simulations. The pressure loss at the rear of the wheel is slightly lowered for the porous fairings compared to the solid one, whereas the points of lowest pressure move forward for all fairing configurations compared to the non-fairing baseline. The mean field of the streamwise velocity component $\overline{u}$ is extracted on a xz-slice through the LG axle and shown in fig. 13 for the four configurations. Considering the length and width of wake sections shown, the configurations agree very well with the experimental results. With increasing porosity of the fairing the separation on the wheel becomes larger and the LG's wake becomes wider.

On the same slice the root mean square (RMS) field of the fluctuating velocity component RMS(u') is given in fig. 13. Slight discrepancy is observed for the baseline configuration between the numerical and experimental results as the flow coming from the wheels is stronger fluctuating in the numerical simulation. The configurations with fairing match very well with the experimental measurements. With increasing porosity of the fairing applied, the RMS(u') value in this slice grows around the wheels as well as in the center of the wake. In fig. 14, a more quantitative comparison is given by plotting the mean and RMS values extracted on specific lines, namley, the x-axis and a line parallel to the z-axis located downstream at $x/D = 1.13$ reinforcing the previous observations.

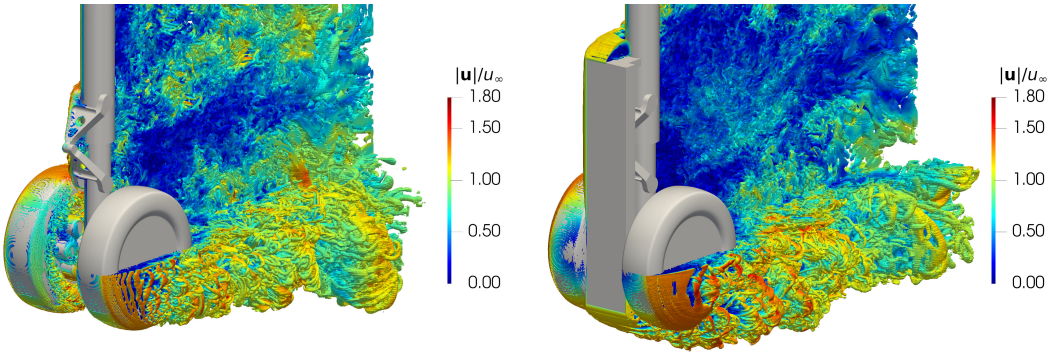

Figure 11: Instantaneous velocity magnitude field on isovolumes of Q-criterion for the baseline (left) and baseline with solid fairing (right) configurations.

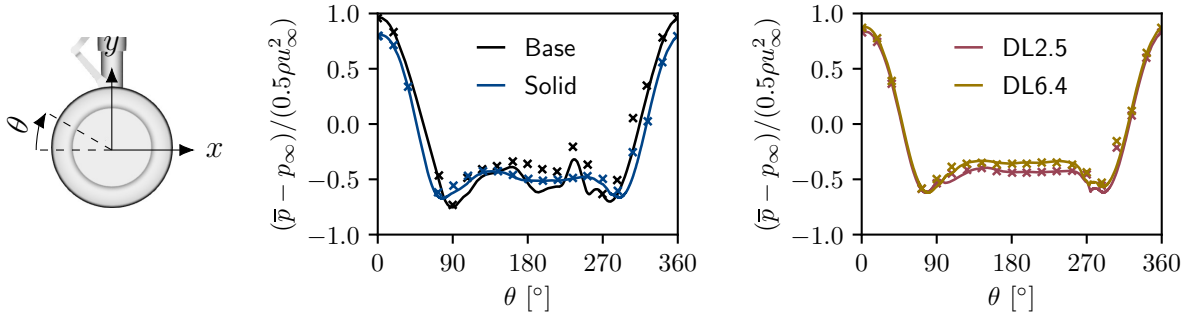

Figure 12: Mean pressure circumferential distribution over the left LG wheel for the four configurations. The corresponding experimental results are given by crosses of the same color. The coordinate system is sketched on the left.

4.2.3 Noise Mitigation Properties of the investigated Fairings

As shown in the previous section the presented numerical approach including the modeling of the porous fairings is capable of reproducing the flow field statistics obtained from experimental PIV measurements. In this section the acoustic far field generated by the different configurations is presented and noise source are discussed.

Two microphones positioned in a distance of $7D$ fylover and $9D$ sideline as sketched in fig. 15 are considered in the following. First, the sound pressure levels predicted by the

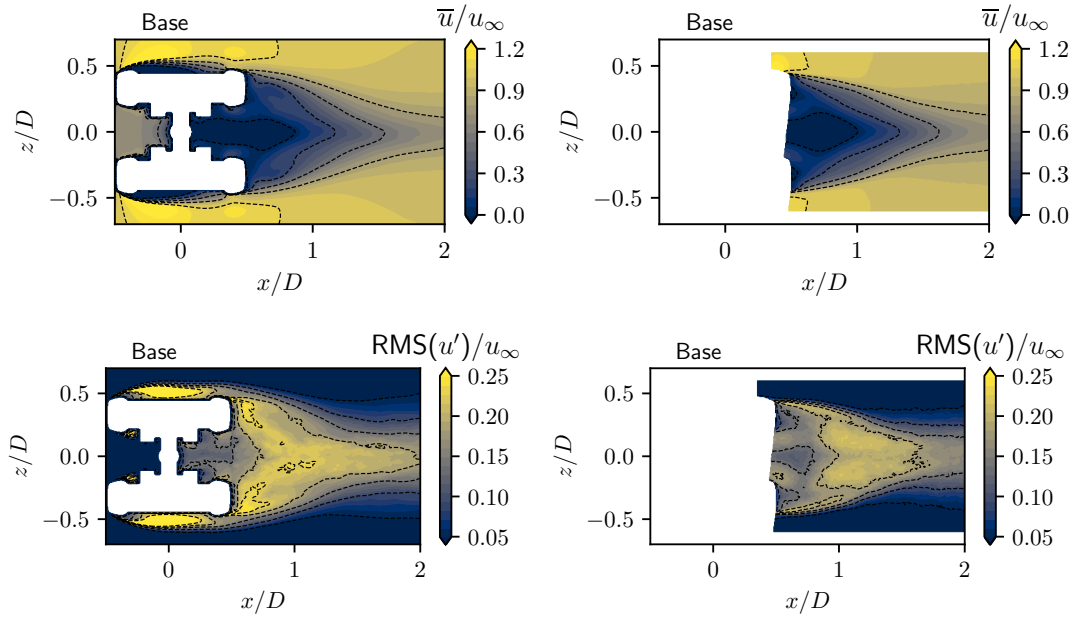

Figure 13: Mean field of the streamwise velocity (top) and root mean square field of fluctuating streamwise velocity (bottom) on an xz-slice through the LG axle. The numerical results (left) are compared to the experimental results of Delft University of Technology (right) for the base configuration without fairing.

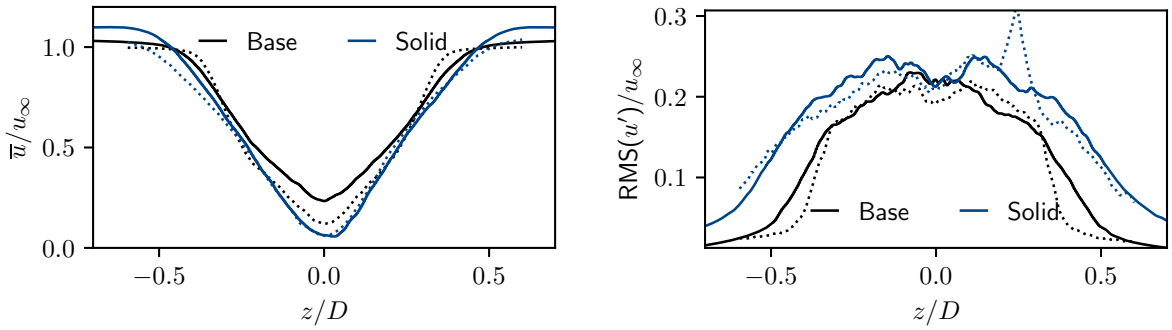

Figure 14: Mean streamwise velocity (left) and root mean square of the fluctuating streamwise velocity (right) on a line parallel to the z-axis located downstream at $x/D = 1.13$ for the base and the solid fairing. The corresponding experimental results are given by dotted lines of the same color.

FW-H calculation are compared to experimental results as well as to an existing numerical study of Terracol et al. Terracol et al. 2023 for the baseline configuration, see fig. 16. The numerical result differ from the experimental ones by approx. 5 dB with a comparable error as in the referred study showing a lower cut-off frequency. This strong discrepancy allows a comparison of the noise reduction capabilities of the applied fairings only on a qualitative point of view. However, in fig. 16 the predicted sound pressure levels of the different configuration are plotted for the two microphones. All fairings show a noise

reduction of approx. 3 dB over a wide range of frequencies. At the sideline position the porous fairings perform similar as the solid version, while in the flyover location the *DL6.4* fairing show better mitigation in the mid frequency range.

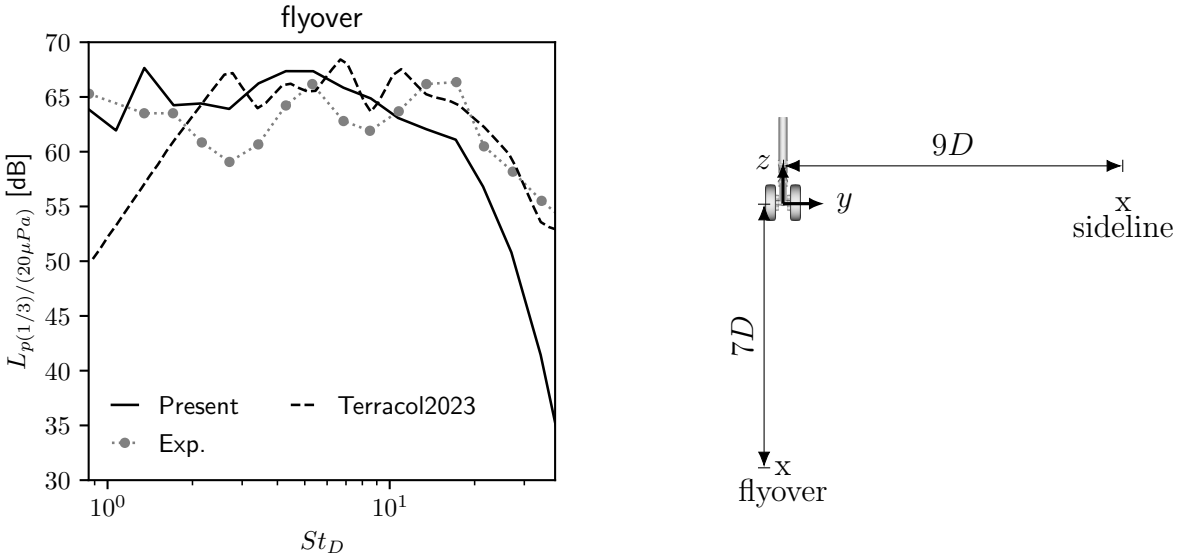

Figure 15: Sound pressure level filtered in one-third octave bands at the sideline microphone position for the base line configuration showing results from the present study as well as from Terracol et al. Terracol et al. 2023 and the experiment. The location of the microphones used in this study are sketched on the right.

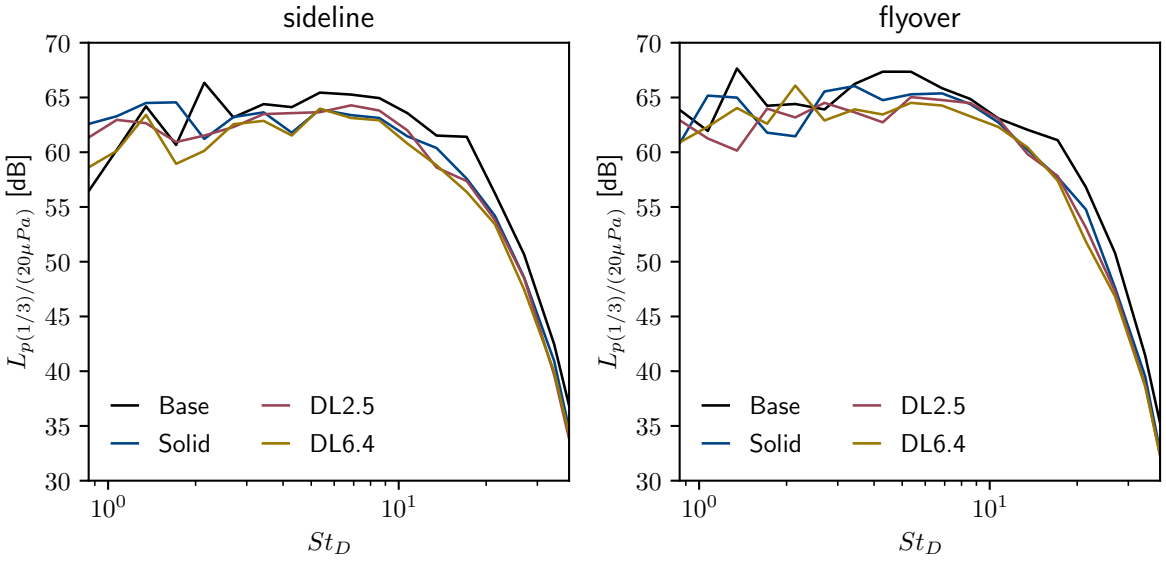

Figure 16: Sound pressure level filtered in one-third octave bands at the two microphone positions for the different landing gear configuration.

4.3 Jet Noise Prediction for Chevron Nozzles

Propulsion system based on gas turbines generate jets for the propulsion of aircraft. Jet noise can be one of the dominant noise sources. This use case illustrates the application of a direct coupled FV/DG solver plus the FW-H method to predict the far field noise.

In the following, cold jets exhausting from the NASA Glenn nozzles SMC000 and SMC006 Bridges and Brown 2004 shown in fig. 17 are considered. The SMC000 nozzle is a baseline configuration without serrations, while the SMC006 chevron nozzle consists of six symmetric lobes with penetration angle 18.2° into the jet stream. The flow conditions are chosen according to the test point 7 of Tanna Tanna 1977, i.e., the jet temperature related to the ambient temperature $T_j/T_\infty = 0.84$ and an acoustic Mach number based on the jet exit velocity of $M_{ac} = U_j/c_\infty = 0.9$. The nozzle exit diameter based Reynolds number is $\mathrm{Re}_D = 400{,}000$.

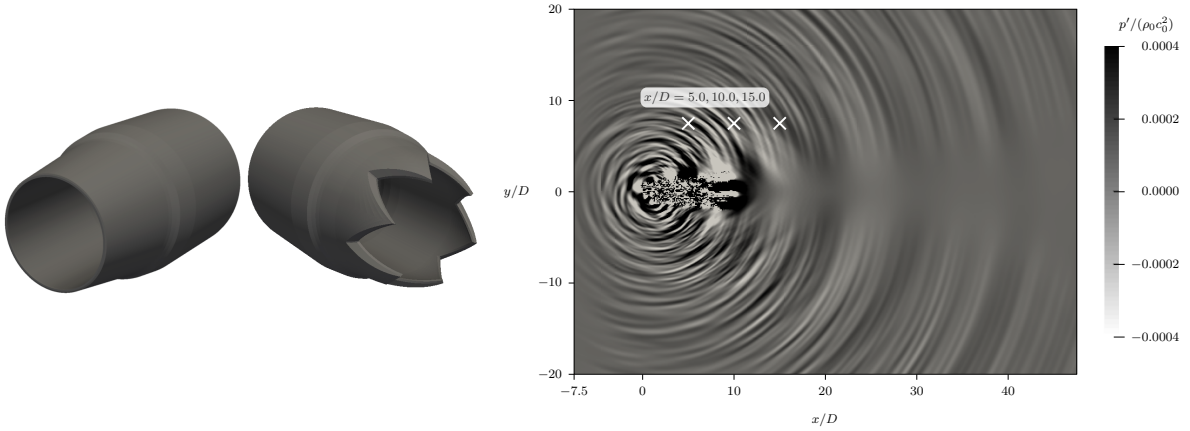

Figure 17: Left: Geometries of NASA Glenn nozzles SMC000 (left) and SMC006 (right) Bridges and Brown 2004. Right: Acoustic pressure field for the SMC006 nozzle in the x-y-plane and observer locations at a radial distance of $r/D = 7.5$.

The flow dynamics and the resulting acoustic field for these jet flow configurations have been previously predicted using a standard hybrid approach Pauz et al. 2017, which utilizes the same large eddy simulation (LES) solver employed in this study. In the acoustics simulation, the acoustic perturbation equations (APE) were solved on a structured mesh utilizing a seven-point finite-difference scheme that preserves the dispersion relation. The temporal integration was carried out using an alternating 5-6 stage low-dispersion, low-dissipation Runge-Kutta method. This methodology has been extensively applied in various aeroacoustic applications, making it an appropriate choice for validating the effectiveness of the direct-hybrid method in chevron nozzle jet aeroacoustics.

To facilitate a direct comparison between the predicted acoustic pressure fields generated by the direct-hybrid method and the reference data, the numerical setup for the computational fluid dynamics (CFD) simulation is designed to closely resemble that of Pauz et al. 2017. The full chevron nozzle model comprises approximately 170 million grid cells. The computational domain extends $48D$ in the streamwise direction and $36D$ laterally. The finest grid resolution of $\Delta/D = 0.0156$ is employed in the acoustic source region, which begins at the nozzle exit and extends $10D$ downstream and $5.5D$ in the lateral direction. To mitigate the generation of spurious noise, a damping zone is implemented

at the boundaries of this region, featuring a smooth transition of the source term amplitudes toward zero. In the computational aeroacoustics (CAA) simulation, the cells within the source region are configured with a spatial resolution that is four times lower. The discontinuous Galerkin (DG) scheme utilizes a polynomial degree of $p = 3$, resulting in approximately 350 million degrees of freedom. Consequently, for transferring the coupling source terms, 64 CFD cells are mapped to the higher-order solution representation of a single CAA element.

Radiation boundary conditions are applied to the outer boundaries, which permit impinging waves to exit the domain while minimizing reflections. Figure 17 illustrates a snapshot of the predicted acoustic field for the SMC006 chevron nozzle. The pressure signal is recorded with a sampling interval of $\Delta t_s c_0/D = 0.0025$ on circles of radius $r/D = 7.5$, positioned along the jet centerline. The total sampling time amounts to $T_{s,a} c_0/D = 164$, commencing at the simulation time $t_a c_0/D = 24$. The power spectral density (PSD) of the acoustic pressure fluctuations is estimated using Welch's method, which divides the data into 15 segments with a 50% overlap. The resulting spectra are averaged for each axial location.

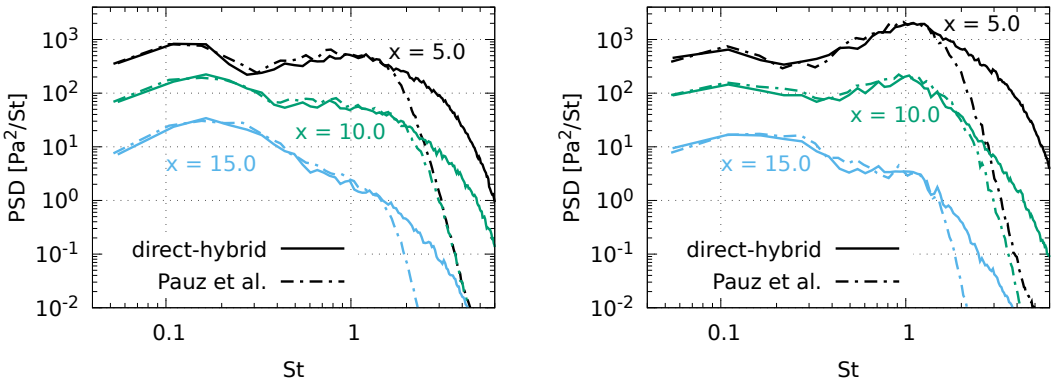

Figure 18: Power spectral density (PSD) of the acoustic pressure versus the Strouhal number St for the nozzles SMC000 (left) and SMC006 (right) at the radial distance $r/D = 7.5$ for $x/D = 5.0$ (a) and (b), $x/D = 10.0$ (c) and (d), and $x/D = 15.0$ (e) and (f) with reference data computed by a standard hybrid scheme from Pauz et al. Pauz et al. 2017. Results for $x/D = 10.0$ and 15 are scaled down by one and two orders of magnitude respectively.

In fig. 18 the computed power spectra for the SMC000 and the SMC006 nozzle are plotted over the Strouhal number $\mathrm{St} = fD/U_j$. The comparison with the reference data shows the three axial locations $x/D = 5.0$, 10.0, and 15.0 in the sideline of the jet, with $x/D = 0.0$ corresponding to the nozzle exit plane. Overall, the power spectra obtained by the direct-hybrid method closely correspond to the reference data. The low frequency range is accurately captured. For the SMC000 nozzle a high increase of the PSD at low Strouhal numbers $\mathrm{St} < 0.4$ is observed at locations farther downstream. In contrast, this trend is less pronounced for the SMC006 chevron nozzle.

Even though there are some small deviations between the results in the frequency range $0.4 < \mathrm{St} < 1.5$, the shapes of the power spectra are in good agreement. That is, a reduction in the high frequency noise with increasing distance to the nozzle exit is visible

for both nozzles. Furthermore, comparing the two nozzle configurations it is evident that the SMC006 nozzle generates significantly more high-frequency noise in comparison to the baseline case.

For Strouhal numbers St > 1.5, the standard hybrid approach shows a rapid decay of the power spectral density. In contrast, this decay is less pronounced in the direct-hybrid method, especially for the axial location $x/D = 5.0$. The direct-hybrid numerical setup provides a higher spatial and temporal resolution, which allows to better resolve the high-frequency noise components propagating normal to the jet axis. In summary, the results confirm the capability of the direct-hybrid method to predict noise from chevron nozzles.

4.3.1 Acoustic Far-Field

The direct-hybrid method allows the prediction of the noise generation and its propagation into the homogeneous near far-field. However, in real world applications or experimental investigations usually the acoustic far-field is of interest to analyze the generated noise and e.g. determine the suitability of shape modifications such as chevrons for noise reduction. To extend the prediction capabilities of the direct-hybrid method the approach can be extended by an integral acoustic method such as the FW-H method. That is, the acoustic variables which are determined by the solution of the APE-4 equations (eqs. (7) and (8)) by the DGSEM need to be sampled on a discretized surface enclosing the acoustic source region such that the time signals can be used as an input to the FW-H equation.

In the following the chevron nozzle SMC001 is considered. It is obtained from the baseline SMC000 nozzle with a 5° contraction angle by cutting out six symmetric lobes. The flow conditions are the same as before, however the Reynolds number now is $\mathrm{Re}_D = 1 \times 10^6$ to match the experimental investigations. In fig. 19 the numerical grids used for the CFD and CAA simulations are illustrated showing the refinement levels in a slice through the whole domain. The domain extends are $52D \times 40D \times 40D$ for the CFD and $65D \times 40D \times 40D$ for the CAA simulation. For the CFD grid conical refinement patches are used to successively increase the grid resolution. The highest spatial resolution to resolve the chevron nozzle wall and the region containing the initial shear layer over an extend of $6D$ downstream the nozzle exit is $\Delta x/D = 0.0039$. Overall the CFD grid consists of about 2.1×10^9 cells. The CAA grid which is composed of a series of cylindrical refinement patches with the highest grid level containing the acoustic source region defined by $(x/D, y/D, z/D) \in [0.2, 22.7] \times [-3.75, 3.75] \times [-3.75, 3.75]$. The corresponding grid spacing is $\Delta/D = 0.0312$ and the polynomial degree for the DG-scheme is $p = 3$. The total number of DOF for the CAA solution representation is 4.97×10^9. To compute the acoustic far-field, a highly-resolved surface is positioned within the acoustic near-field of the computational aeroacoustics (CAA) simulation, where time-resolved data is gathered. This surface is conical in shape, commencing with a radius of $2.5D$ at an axial location of $5D$ upstream from the nozzle exit, and linearly expanding to $6D$ over a downstream distance of $35D$. The surface is open in the upstream direction and closed in the downstream direction. In total, the surface area is discretized into approximately 3.9×10^6 triangular surface elements, which corresponds to an average element surface area of $2.7 \times 10^{-4} D^2$.

The sampling interval is set to $\Delta t_{samp} = 0.015 D/c_0$, and the total sampling time allocated for the FW-H far-field prediction is about $430 D/c_0$. Welch's method is utilized

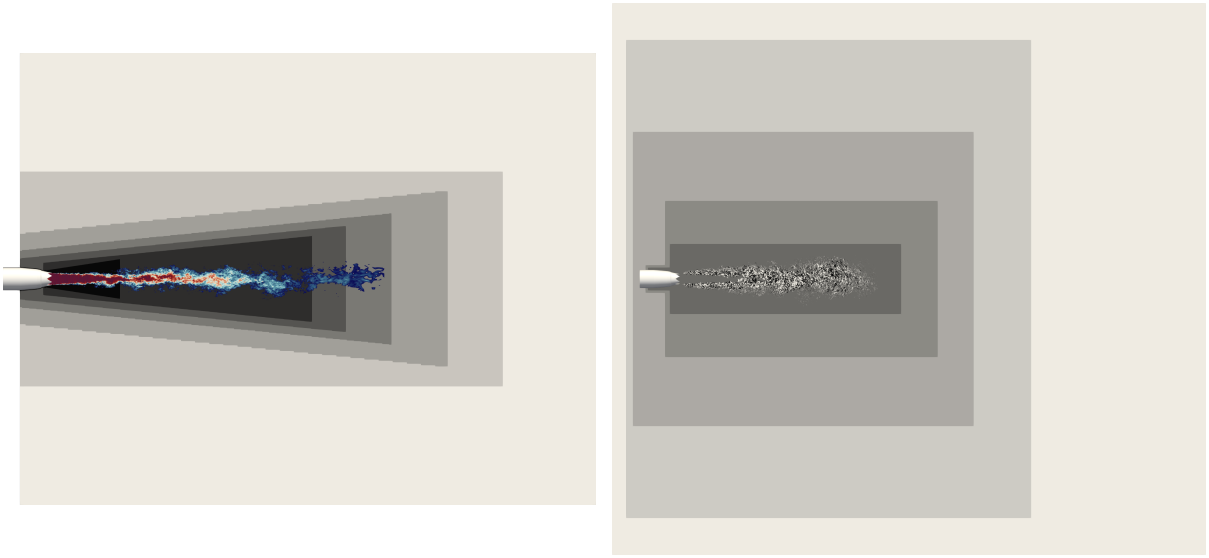

Figure 19: Left: Slice through CFD domain showing increasingly refined grid levels from coarse (light grey) to fine (black). Right: Slice through CAA domain showing increasingly refined grid levels from coarse (light grey) to fine (dark grey). Visualization of instantaneous acoustic source term L_y in acoustic source region

for the estimation of the power spectral density (PSD), segmenting the total time signal into 7 segments, each containing 4096 samples. Acoustic far-field observers are positioned along an arc with a radius of $100D$. For each angle, a total of 72 points in the azimuthal direction are computed, and the spectra are averaged.

In fig. 20, the predicted power spectral densities for two observer angles, 45° and 75°, are compared against reference data derived from experimental consensus as well as numerical results from Stich et al. 2020. The results demonstrate a strong agreement with the reference data across a wide frequency range.

4.4 Propeller-Airfoil Interaction Noise

Propellers are typically used for small aircrafts or drones and constitute a major noise source. In this use case, the acoustic field of rotating propellers is predicted using a FV method coupled with a FW-H approach. The results shown in this section were obtained in the EU project ENODISE.

The test geometry utilized is the ENODISE-B1 configuration, supplied by the Technische Universiteit Delft (TUD) Nascimento Monteiro et al. 2023, which is illustrated in fig. 21. This setup features three XPROP-S propellers arranged side-by-side, positioned upstream of the leading edge of a wing. Each XPROP-S propeller consists of six blades and has a diameter of $D = 203.2$ mm. At 70% of the radius, the blade pitch angle is set to $\beta_{0.7R} = 30°$, while the blade chord length at this radius is $c_{0.7R} = 15.5$ mm. The propellers are located approximately $0.85D$ upstream of the wing's leading edge, with a shaft incidence angle of $i_{prop} = -5°$ relative to the wing chord. Additionally, the tip clearance between adjacent propellers measures $d = 4.8$ mm. The wing itself features a NLF-Mod22(B) profile, with a chord length of $c_{wing} = 300$ mm and a span of 1248 mm.

The incoming freestream velocity is set to $U_\infty = 30$ m/s, with a wing angle of attack

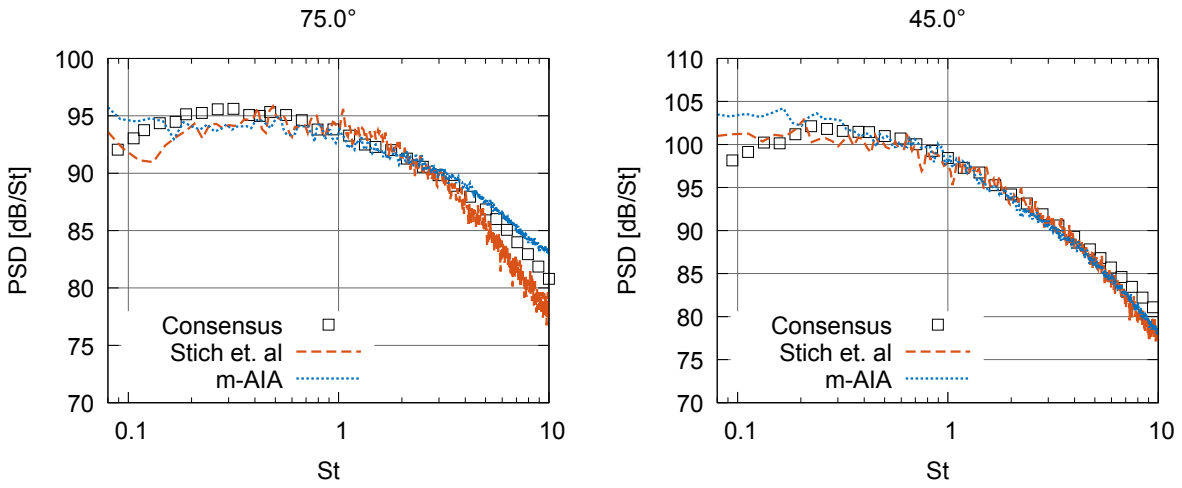

Figure 20: Comparison of acoustic far-field power spectral density at a distance of $100D$, an angle of 0° corresponds to the downstream direction. Left: observer angle 75°. Right: observer angle 45°.

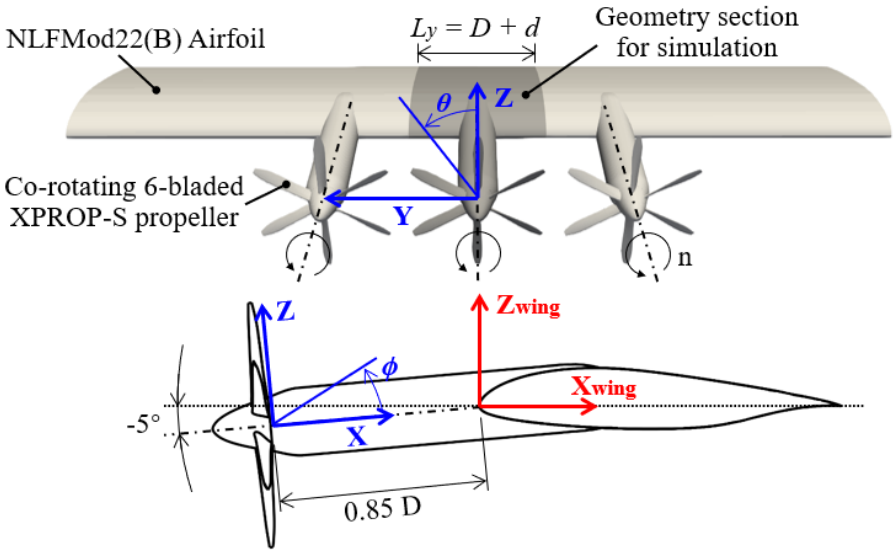

Figure 21: Geometry of the test setup

of $AoA = 2°$. The Reynolds number, calculated based on the wing's chord length, is approximately $Re_{wing} = 6 \cdot 10^5$. The three propellers are rotating with a zero relative blade phase angle at a speed of $n = 11073$ rpm. This results in a blade tip tangential Mach number of about $M_{tip} = 0.35$, a blade passing frequency of $BPF = 1107$ Hz, and a propeller advance ratio of $J = \frac{U_\infty}{nD} = 0.8$.

To minimize computational costs, periodic boundary conditions are implemented between the tip gaps of adjacent propellers, as observed by Vries et al. 2021. In the computational domain, only the middle propeller is explicitly resolved, as indicated by the dark gray representation in fig. 21. A periodic condition is applied to the spanwise (Y-direction) boundary of the domain to capture the effects of the propellers on both

neighboring sides. This approach allows for a significant reduction in the spanwise extent of the simulation, effectively simulating an infinite array of propellers, evenly distributed side by side and synchronized at the same rotational speed and phase angle. The computational domain is configured as a box with dimensions $L_x = 12D$, $L_y = D + d$, and $L_z = 6D$. A no-slip boundary condition is enforced on all surfaces, which are assumed to be adiabatic. Subsonic inlet and outlet conditions are applied at the far-field boundaries, incorporating an acoustic sponge layer to absorb any pressure waves reflecting inward.

The computational mesh is shown in fig. 22. To resolve the turbulent boundary layer near the solid surfaces, the minimum spatial step near solid surfaces is chosen to be $7 \cdot 10^{-5}$ m. Approximately 200 cells are distributed along the propeller chord and 4,000 cells along the wing chord. Adaptive mesh refinement is applied to the fluid-solid interface with the minimum spatial resolution and coarsening towards the far field until a maximum spatial step of $2 \cdot 10^{-3}$ m is reached. Patch refinement boxes are implemented in the near field to better resolve the propeller slipstream and the airfoil wake. Overall, this leads to approximately $1.5 \cdot 10^9$ grid cells. The rotating propeller and the high-frequency turbulent scales are resolved with a time step of $1 \cdot 10^{-7}$ s, which is determined by the stability limit of the numerical method.

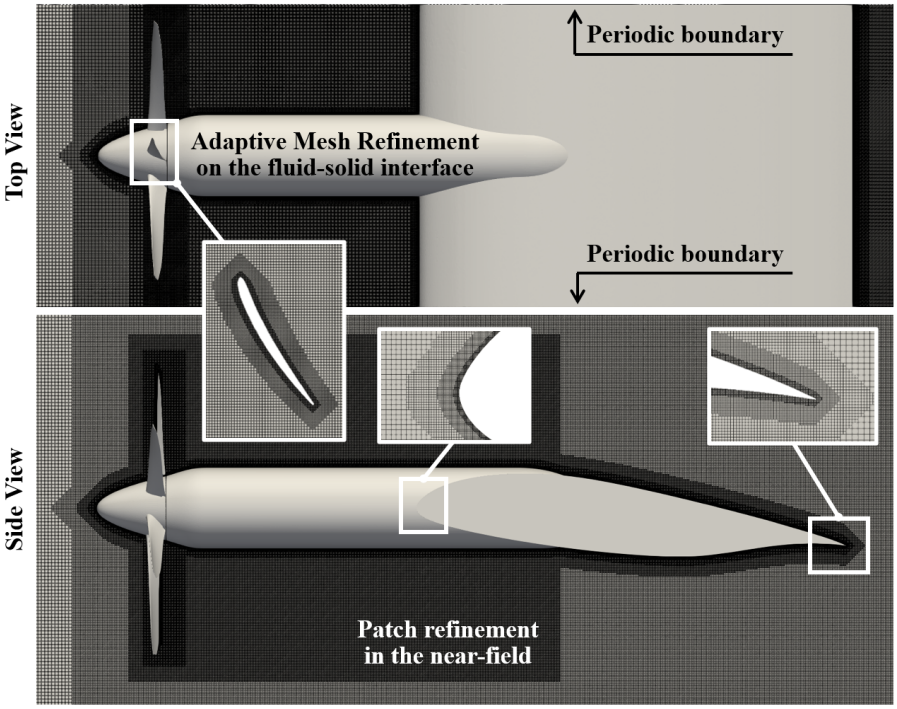

Figure 22: Illustration of the mesh

Figure 23 shows the permeable FW-H surface superimposed on the instantaneous solution of the installed ENODISE-B1 configuration. It consists of a set of blue surfaces surrounding the propeller slipstream to include most of the noise sources. The Y-direction sides of the FW-H surface are open due to the periodic boundary conditions, and the downstream surface is left open to avoid spurious noise generated by hydrodynamic perturbations traveling over the sampling surface. The spatial resolution of the sampling surface is $2 \cdot 10^{-3}$ m, and the sampling frequency is also 85 kHz, and data for 5 propeller

revolutions are recorded. After the samples are recorded, the FW-H surface is duplicated to generate in total three copies and arranged side by side around three propellers to calculate the far-field noise of the three-propeller configuration.

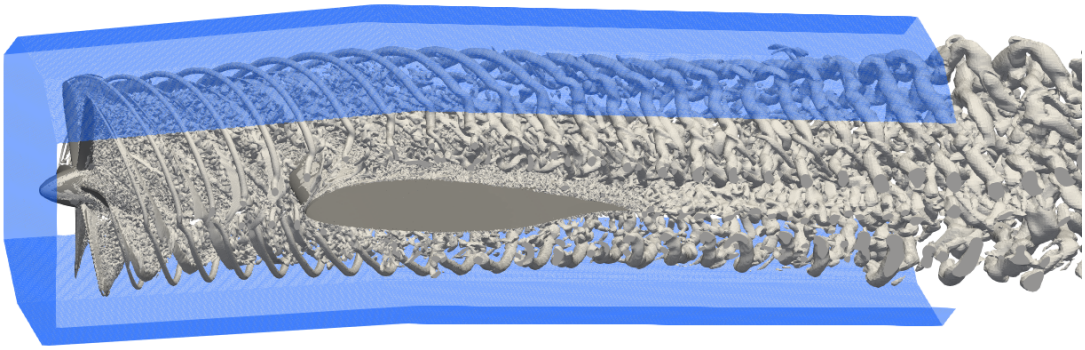

Figure 23: Location of the permeable FW-H sampling surface in the installed configuration. The near-field vortex structures are determined by the Q-Criterion with iso-surface of $\tilde{Q} = 1$.

Figure 24 compares the distribution of the total pressure coefficient $C_{pT} = (p_T - p_\infty)/(0.5\rho_\infty U_\infty^2)$ two chord lengths downstream of the wing. The LES results agree with the total pressure coefficient measured in the experiment by TUD, indicating that the numerical method can accurately predict the viscous near field of the installed distributed propellers.

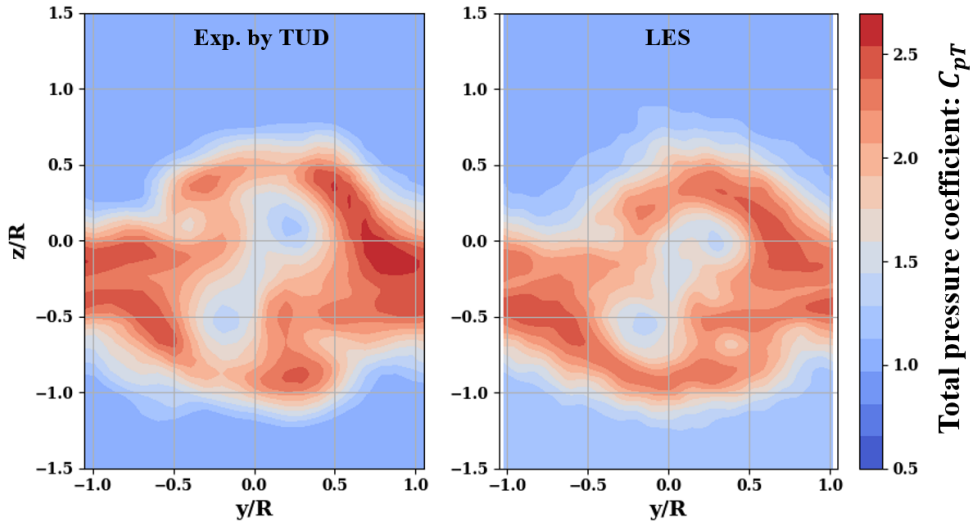

Figure 24: Total pressure coefficient in the wake of the wing.

The predicted far-field noise spectra of the periodic installed configuration are compared with experimental data of the three-propeller setup obtained by TUD in fig. 25. According to the experimental setups, 64 microphones are placed on the plane 1.05 m off the wing surface. Two representative microphone positions are selected for validation, including the upstream (Mic A) and downstream (Mic B) locations. The power spectral density (PSD) of the acoustic signal is calculated using Welch's method, 50% overlap,

filtered by a Hanning window, with a frequency resolution of $\Delta f = 6.25\ Hz$, and the reference pressure is $2 \cdot 10^{-5}\ Pa$. The grey dashed lines in the plots represent the propeller blade passing frequency (BPF) and its harmonics.

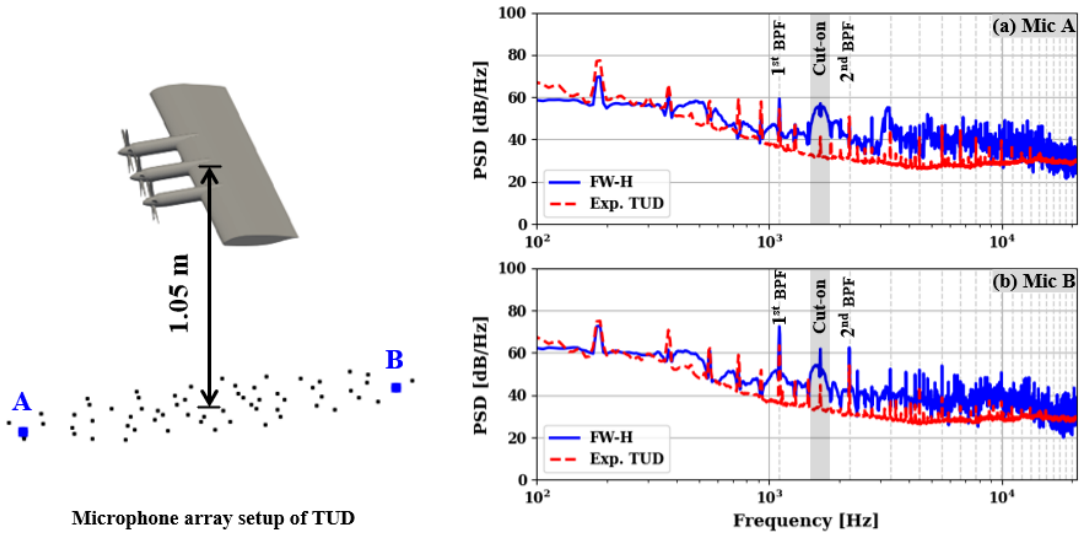

Figure 25: Comparison of the predicted power spectral density of the far-field noise with experimental data.

As illustrated in fig. 25, the FW-H predictions demonstrate good agreement with the experimental results for broadband noise across the frequency range of 100 Hz to 20 kHz. For tonal noise, the first and second blade passing frequencies (BPF) of the propeller are indicated in the plot, occurring at approximately 1107 Hz and 2214 Hz, respectively. The FW-H predictions align well with the reference values at the upstream microphone A, as shown in fig. 25(a), while they overpredict the tonal noise at the downstream microphone B in fig. 25(b). This overprediction can be attributed to the periodic simulation setup, which effectively incorporates noise signals from an infinite array of propellers in the spanwise direction, leading to an elevation in the noise level. Furthermore, the periodic boundary conditions employed in the spanwise direction during the numerical simulation tend to amplify modes with wavelengths on the order of the spanwise extent. This phenomenon is characterized by what is referred to as the cut-on frequency Soni et al. 2022. In the present simulations, the cut-on frequency is determined to be $f_c = c_0/L_y = 1634$ Hz. Consequently, noise spectra near f_c and its higher harmonics experience amplification.

4.5 Propeller-Propeller Interaction Noise

For distributed propulsion systems with small propeller installation tip gaps, the aerodynamic/aeroacoustic interactions between adjacent propellers become prominent which could lead to a significant increase in propeller unsteady loading noise.

Turhan et al. 2024 has developed an experimental setup, shown in fig. 21(left), to investigate the interaction noise of the closely arranged distributed propellers and evaluate the effectiveness of phase-synchronization for propeller noise reduction. The experiments were performed with two 2-bladed propellers manufactured by Mejzlik, with a diameter of $D = 228.6\ mm$ (9 inch) and a pitch-to-diameter ratio of $P/D = 1$. The center-to-center

separation distance between adjacent propellers is $S/D = 1.05$. The two propellers were mounted 150 mm upstream of a supportive airfoil with a NACA0018 profile, a chord length of $c_{wing} = 300$ mm, and a span of 940 mm.

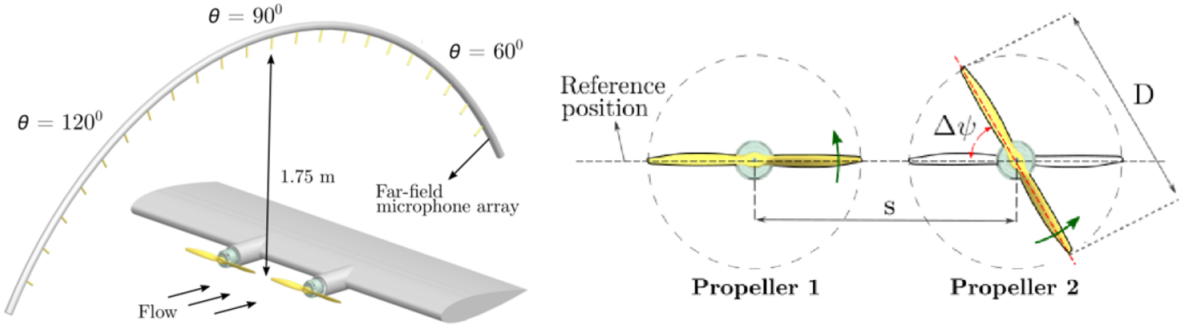

(a) Test Geometry **(b) Definition of the reference system**

Figure 26: Experimental setup for propeller-propeller interaction noise.

The incoming freestream velocity is $U_\infty = 10$ m/s with a wing angle of attack $AoA = 0°$. The Reynolds number based on the wing chord length is approximately $Re_{wing} = 2{\cdot}10^5$. The two propellers are rotating in the same direction at the speed of $n = 5000$ rpm, giving a blade tip tangential Mach number of about $M_{tip} = 0.17$, a blade passing frequency of $BPF = 166.7$ Hz and a propeller advance ratio of $J = U_\infty/(nD) = 0.53$. Two propeller blade relative phase angle, $\Delta\psi = 0°$ and $90°$ is tested.

Based on the previous experimental/numerical observations by Sinnige et al. 2019; Zhe, Meinke, and Schröder 2024 that the propeller-propeller interaction is a major noise source of the distributed propulsion system and has a much higher contribution to the far-field noise than the propeller-airfoil interaction, therefore, the simulation only involves the co-rotating propeller pairs. The supportive nacelle and airfoil are omitted from the simulation to reduce the computational costs. The computational domain is set to be a box with the lengths $L_x = 1400$ mm, $L_y = 1200$ mm, and $L_z = 1000$ mm. The no-slip boundary condition is imposed on all surfaces which are assumed to be adiabatic. Subsonic inlet and outlet conditions with an acoustic sponge layer are used for the far-field boundaries to absorb any inward-reflecting pressure waves.

The computational mesh is shown in fig. 27. To resolve the turbulent boundary layer near the solid surfaces, the minimum spatial step near solid surfaces is chosen to be $4.3 \cdot 10^{-5}$ m. Approximately 300 cells are distributed along the propeller chord. Adaptive mesh refinement is applied to the fluid-solid interface with the minimum spatial resolution and coarsening towards the far field until a maximum spatial step of $1.4{\cdot}10^{-3}$ m is reached. Patch refinement boxes are implemented in the near field to better resolve the propeller slipstream. Overall, this leads to approximately $500 \cdot 10^6$ grid cells. The rotating propeller and the high-frequency turbulent scales are resolved with a time step of $1 \cdot 10^{-7}$ s, which is determined by the stability limit of the numerical method.

Similar to section 4.4, a permeable FW-H surface around the vortex core of the co-rotating propeller pairs is employed to record the near-field perturbations. The downstream side of the FW-H surface is left open to avoid spurious noise generated by hydrodynamic perturbations traveling over the sampling surface. The spatial resolution of the

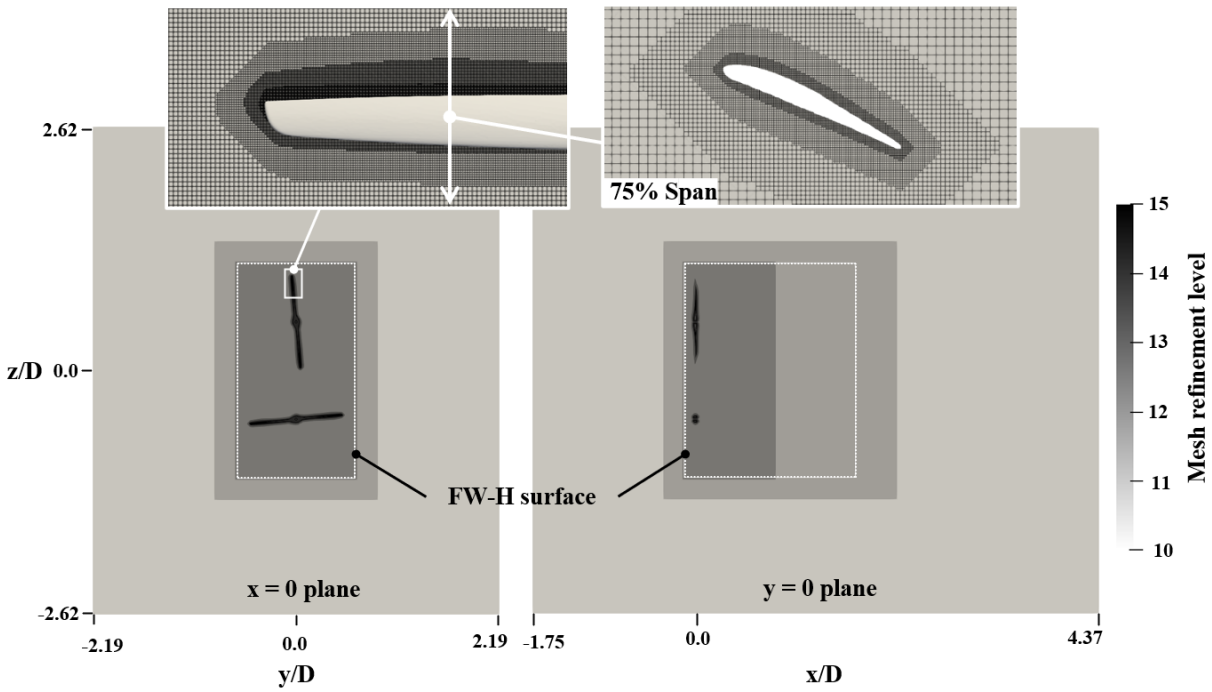

Figure 27: Illustration of the computational domain and mesh

sampling surface is $2 \cdot 10^{-3}$ m, and the sampling frequency is also 65 kHz, and data for 10 propeller revolutions are recorded.

The instantaneous vortex structures of the co-rotating propeller pairs with relative phase angle $\Delta\psi = 0°$ are shown in fig. 28. It illustrates the generation and propagation of the propeller tip vortices.

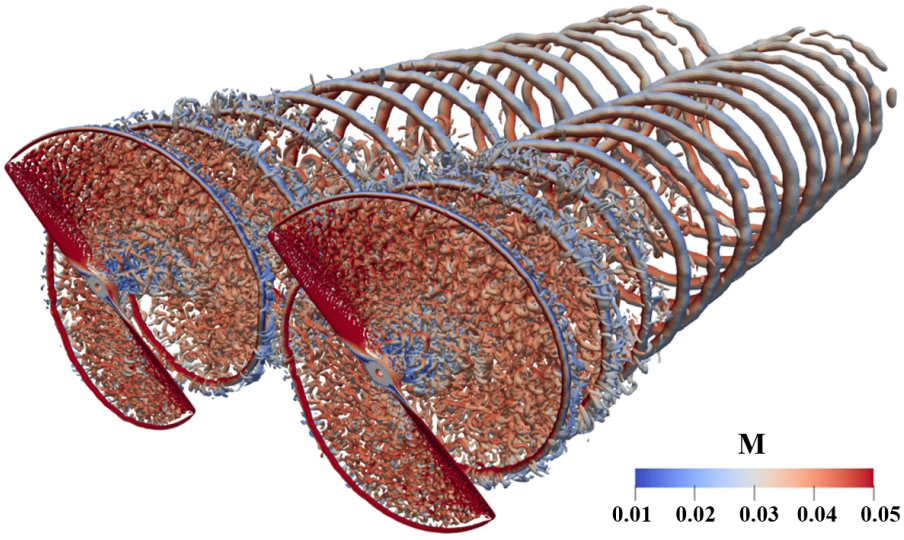

Figure 28: Vortex structures denoted by the Q-Criterion with an iso-surface value of $\tilde{Q} = 2$.

The far-field noise of the synchronized propellers is calculated by the permeable FW-

H approach and compared with the wind tunnel measurements from Turhan et al. 2024. The microphone is located 1.75 m away from the propeller in the vertical plane with an angular position of $\theta = 90°$. The power spectral density (PSD) of the acoustic signal is calculated using Welch's method, 50% overlap, filtered by a Hanning window, with a frequency resolution of $\Delta f = 1.0\ Hz$, and the reference pressure is $2 \cdot 10^{-5}\ Pa$. The grey dashed lines in the plots represent the propeller blade passing frequency (BPF) and its harmonics.

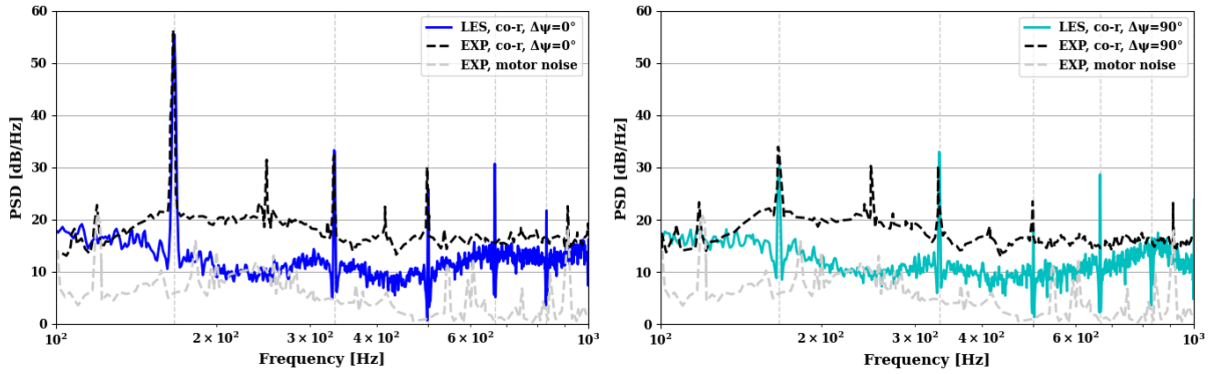

(a) $\Delta\psi = 0°$ **(b) $\Delta\psi = 90°$**

Figure 29: Predicted power spectral density of the co-rotating propeller pairs with relative phase angle (a) $\Delta\psi = 0°$ (b) $\Delta\psi = 90°$

Figure 29 compares the predicted far-field noise spectra with the experimental reference data in the frequency range from 100 Hz to 1000 Hz. It can be seen that the propeller tonal noise at the first and second BPF frequencies is accurately predicted by the numerical method. The reference data showed a higher amplitude of broadband noise, which was mainly caused by the background motor noise in the wind tunnel experiment. Further, a more than 20 dB reduction in the propellers' first BPF tonal noise can be found from the relative phase angle $\Delta\psi = 90°$ case, indicating the propeller phase synchronization technique could provide an effective means of tonal noise reduction.

5 Conclusions

This paper presents various methodologies for the simulation of aeroacoustic problems based on unsteady simulations of the flow field. In the use cases included here, the acoustic field is obtained from the unsteady flow field using

- a CAA method based on solving the acoustic perturbation equations
- an integral method such as the FW-H method

Both methods have their own advantages and disadvantages. In case the main source term driving the acoustic wave generation is the perturbed Lamb vector, the properties of the two methods can be summarized in the following:

- CAA solving the APE
  - \+ generation of the acoustic waves in the acoustic source region, i.e., the CFD solution does not need to be predict acoustic wave propagation
  - \+ Not very sensitive to a contaminated CFD solution by small pressure oscillations, e.g. from wave reflections at an outflow boundary
  - \+ Can be combined with a FW-H method to obtain the acoustic far field
  - – Coupling of two Eulerian solvers is required
  - – Relatively high computational effort
  - – Formulation for rotating objects in a fixed frame of reference not available yet
- FW-H method
  - \+ Acoustic far field can be obtained in a postprocessing step
  - \+ Relatively small computational effort
  - – When a permeable FW-H surface is used, the CFD solver has to accurately predict acoustic wave propagation until the surface is reached
  - – Results may depend on the location of the FW-H surface
  - – Fluid dynamic pressure fluctuation crossing the FW-H surface may generate artificial noise

The correct prediction of the acoustic far field noise based on scale resolving simulations still requires extensive experience, testing and validation. The use cases presented in the paper are made available in Institute of Aerodynamics, RWTH Aachen University 2024b and hopefully help to set up solutions for other problems.

6 Acknowledgement

The funding of the European Union's Horizon 2020 research and innovation program within the project ENODISE (Enabling optimized disruptive airframe-propulsion integration concepts) (www.vki.ac.be/index.php/about-enodise) grant agreement No.860103 and the project INVENTOR (innovative design of installed airframe components for aircraft noise reduction) listed under the grant agreement No.860538 is gratefully acknowledged. The funding of the European High-Performance Computing Joint Undertaking (JU) within the COE EXCELLERAT P2 under grant agreement No 101092621 is gratefully acknowledged. The JU receives support from the European Union's Horizon Europe research and innovation programme and Germany, Italy, Slovenia, Spain, Sweden and France. The authors finally gratefully acknowledge the Gauss Centre for Supercomputing e.V. (www.gauss-centre.eu) for funding this project by providing computing time on the GCS Supercomputer HAWK at Höchstleistungsrechenzentrum Stuttgart (www.hlrs.de) and GCS Supercomputer JUWELS at Jülich Supercomputing Centre (JSC).

References

Angot, P., Bruneau, C.-H., and Fabrie, P. (1999). "A penalization method to take into account obstacles in incompressible viscous flows". In: *Numerische Mathematik* 81.4, pp. 497–520.

Bae, Y. and Moon, Y. J. (2012). "On the use of Brinkman penalization method for computation of acoustic scattering from complex boundaries". In: *Comput. Fluids* 55, pp. 48–56.

Bhatnagar, P. L., Gross, E. P., and Krook, M. (1954). "A Model for Collision Processes in Gases. I. Small Amplitude Processes in Charged and Neutral One-Component Systems". In: *Phys. Rev.* 94 (3), pp. 511–525. DOI: 10.1103/PhysRev.94.511.

Boris, J. P. et al. (1992). "New insights into large eddy simulation". In: *Fluid dynamics research* 10.4-6, p. 199. DOI: 10.1016/0169-5983(92)90023-P.

Bouzidi, M., Firdaouss, M., and Lallemand, P. (2001). "Momentum transfer of a Boltzmann-lattice fluid with boundaries". In: *Phys. Fluids* 13.11, pp. 3452–3459. DOI: 10.1063/1.1399290.

Brentner, K. S. and Farassat, F. (1998). "Analytical comparison of the acoustic analogy and Kirchhoff formulation for moving surfaces". In: *AIAA journal* 36.8, pp. 1379–1386. DOI: 10.2514/2.558.

Brès, G., Pérot, F., and Freed, D. (2010). "A Ffowcs Williams-Hawkings solver for Lattice-Boltzmann based computational aeroacoustics". In: *16th AIAA/CEAS aeroacoustics conference*, p. 3711. DOI: 10.2514/6.2010-3711.

Bridges, J. and Brown, C. (2004). "Parametric testing of chevrons on single flow hot jets". In: *AIAA Paper 2004–2824*. DOI: 10.2514/6.2004-2824.

Carpenter, M. H. and Kennedy, C. A. (1994). *Fourth-order 2N-storage Runge-Kutta schemes*. Tech. rep. NASA/TM-109112. NASA Langley Research Center.

Chung, C. and Morris, P. J. (1998). "Acoustic scattering from two-and three-dimensional bodies". In: *J. Comp. Acoust.* 6.03, pp. 357–375. DOI: doi/10.2514/2.2563.

Dupuis, A. and Chopard, B. (2003). "Theory and applications of an alternative lattice Boltzmann grid refinement algorithm". In: *Phys. Rev. E* 67 (6), p. 066707. DOI: 10.1103/PhysRevE.67.066707.

Enskog, D. (1917). "Kinetische Theorie der Vorgänge in mässig verdünnten Gasen." ger. PhD thesis.

Ewert, R. and Schröder, W. (2003). "Acoustic perturbation equations based on flow decomposition via source filtering". In: *J. Comput. Phys.* 188.2, pp. 365–398. DOI: 10.1016/s0021-9991(03)00168-2.

Fröhlich, K. et al. (2021). "Particle Reynolds number effects on settling ellipsoids in isotropic turbulence". In: *International Journal of Multiphase Flow* 139, p. 103566. DOI: 10.1016/j.ijmultiphaseflow.2021.103566.

Gassner, G. and Kopriva, D. A. (2011). "A comparison of the dispersion and dissipation errors of Gauss and Gauss–Lobatto discontinuous Galerkin spectral element methods". In: *SIAM J. Sci. Comp.* 33.5, pp. 2560–2579.

Geier, M. et al. (2015). "The cumulant lattice Boltzmann equation in three dimensions: Theory and validation". In: *Comp. Math. Applics* 70.4, pp. 507–547. DOI: 10.1016/j.camwa.2015.05.001.

Gondrum, M., Meinke, M., et al. (2024). "Porous Fairings for Landing Gear Noise Mitigation". In: *30th AIAA/CEAS Aeroacoustics Conference (2024)*. DOI: 10.2514/6.2024-3174.

Gondrum, M., Niemöller, A., et al. (2022). "Landing Gear Noise Mitigation by an upstream installed Fairing". In: *28th AIAA/CEAS Aeroacoustics Conference*. American Institute of Aeronautics and Astronautics. DOI: 10.2514/6.2022-2847.

Gondrum, M., Satcunanathan, S., et al. (2023). "A direct-hybrid CFD/CAA method based on lattice Boltzmann and acoustic perturbation equations". In: *Acta Acust* 7, p. 5. DOI: 10.1051/aacus/2022062.

Günther, C., Meinke, M., and Schröder, W. (2014). "A flexible level-set approach for tracking multiple interacting interfaces in embedded boundary methods". In: *Computers & Fluids* 102, pp. 182–202. DOI: 10.1016/j.compfluid.2014.06.023.

Guo, Z. and Zhao, T. S. (2002). "Lattice Boltzmann model for incompressible flows through porous media". In: *Phys. Rev. E* 66 (3), p. 036304. DOI: 10.1103/PhysRevE.66.036304.

Guo, Z., Zheng, C., and Shi, B. (2002). "Discrete lattice effects on the forcing term in the lattice Boltzmann method". In: *Phys. Rev. E* 65 (4), p. 046308. DOI: 10.1103/PhysRevE.65.046308.

Hartmann, D., Meinke, M., and Schröder, W. (2008). "An adaptive multilevel multigrid formulation for Cartesian hierarchical grid methods". In: *Comput. Fluids* 37.9, pp. 1103–1125. ISSN: 0045-7930. DOI: 10.1016/j.compfluid.2007.06.007.

Hindenlang, F. et al. (2012). "Explicit discontinuous Galerkin methods for unsteady problems". In: *Comput. Fluids* 61, pp. 86–93.

Hou, S. et al. (1996). "A Lattice Boltzmann Subgrid Model for High Reynolds Number Flows". In: *Fields Inststitute Communication*. Vol. 6, pp. 151–166.

Hunt, J.C.R., Wray, A. A., and Moin, P. (1988). "Eddies, streams, and convergence zones in turbulent flows". In: *Studying turbulence using numerical simulation databases, 2. Proceedings of the 1988 summer program.*

Inoue, O. and Hatakeyama, N. (2002). "Sound generation by a two-dimensional circular cylinder in a uniform flow". In: *Journal of Fluid Mechanics* 471, pp. 285–314. DOI: 10.1017/S0022112002002124.

Institute of Aerodynamics, RWTH Aachen University (2024a). *m-AIA*. Zenodo. DOI: 10.5281/zenodo.13350586.

— (2024b). *m-AIA Use Cases*. Git Repository. URL: https://git.rwth-aachen.de/aia/m-aia-use-cases.git.

Izquierdo, S. and Fueyo, N. (2008). "Characteristic nonreflecting boundary conditions for open boundaries in lattice Boltzmann methods". In: *Phys. Rev. E* 78 (4), p. 046707. DOI: 10.1103/PhysRevE.78.046707.

Koh, S. R., Schröder, W., and Meinke, M. (2010). "Turbulence and heat excited noise sources in single and coaxial jets". In: *J. Sound Vibr.* 329.7, pp. 786–803. ISSN: 0022-460X. DOI: 10.1016/j.jsv.2009.10.012.

Kopriva, D. A., Woodruff, S. L., and Hussaini, M. Y. (2000). "Discontinuous spectral element approximation of Maxwell's equations". In: *Discontinuous Galerkin Methods*. Springer, pp. 355–361. DOI: doi:10.1007/978-3-642-59721-3_33.

— (2002). "Computation of electromagnetic scattering with a non-conforming discontinuous spectral element method". In: *Int. J. Num. Meth. Eng.* 53.1, pp. 105–122. DOI: 10.1002/nme.394.

Laik, O. A. and Morris, P. J. (2000). "Direct simulation of acoustic scattering by two-and three-dimensional bodies". In: *J. Aircraft* 37.1, pp. 68–75. DOI: 10.2514/2.2563.

Liu, Q. and Vasilyev, O. V. (2007). "A Brinkman Penalization Method for Compressible Flows in Complex Geometries". In: *J. Comput. Phys.* 227, pp. 946–966. DOI: 10.1016/j.jcp.2007.07.037.

Lockard, D.P. (2000). "An efficient, two-dimensional implementation of the Ffowcs Williams and Hawkings equation". In: *J. Sound Vibr.* 229.4, pp. 897–911. ISSN: 0022-460X. DOI: 10.1006/jsvi.1999.2522.

Nascimento Monteiro, F. do et al. (2023). "H2020 ENODISE: TUD Experimental database configuration B1". Version v1.0. In: *Zenodo Database*. DOI: 10.5281/zenodo.8307371.

Pauz, V. et al. (2017). "Numerical analysis of chevron nozzle noise". In: *AIAA Paper 2017–3853*. DOI: 10.2514/6.2017-3853.

Pogorelov, A., Meinke, M., and Schröder, W. (2015). "Cut-cell method based large-eddy simulation of tip-leakage flow". In: *Phys. Fluids* 27.7, p. 075106.

Pogorelov, A., Schneiders, L., et al. (2018). "An adaptive Cartesian mesh based method to simulate turbulent flows of multiple rotating surfaces". In: *Flow, Turbulence and Combustion* 100, pp. 19–38. DOI: 10.1007/s10494-017-9827-9.

Schlottke-Lakemper, M., Niemöller, A., et al. (2019). "Efficient parallelization for volume-coupled multiphysics simulations on hierarchical Cartesian grids". In: *Comp. Meth. Appl. Mech. Eng.* 352, pp. 461–487. ISSN: 0045-7825. DOI: 10.1016/j.cma.2019.04.032.

Schlottke-Lakemper, M., Yu, H., et al. (2017). "A fully coupled hybrid computational aeroacoustics method on hierarchical Cartesian meshes". In: *Comput. Fluids* 144, pp. 137–153. DOI: 10.1016/j.compfluid.2016.12.001.

Schneiders, L., Günther, C., et al. (2016). "An efficient conservative cut-cell method for rigid bodies interacting with viscous compressible flows". In: *Journal of Computational Physics* 311, pp. 62–86. DOI: 10.1016/j.jcp.2016.01.026.

Schneiders, L., Hartmann, D., et al. (2013). "An accurate moving boundary formulation in cut-cell methods". In: *J. Comput. Phys.* 235, pp. 786–809. DOI: 0.1016/j.jcp.2012.09.038.

Sinnige, T. et al. (2019). "Alleviation of propeller-slipstream-induced unsteady pylon loading by a flow-permeable leading edge". In: *Journal of Aircraft* 56.3, pp. 1214–1230. DOI: 10.2514/1.C035250.

Soni, M. et al. (2022). "Towards Wall-Modeled LES with Lattice Boltzmann Method for Aeroacoustics: Application and Understanding". In: *28th AIAA/CEAS Aeroacoustics 2022 Conference*, p. 2918. DOI: 10.2514/6.2022-2918.

Stich, G.-D. et al. (2020). "Jet Noise Prediction for Chevron Nozzle Flows with Wall-Modeled Large-Eddy Simulation". In: *AIAA SciTech Forum 2021*. DOI: 10.2514/6.2021-1185.

Tanna, H. K. (1977). "An experimental study of jet noise Part I: Turbulent mixing noise". In: *J. Sound Vibr.* 50.3, pp. 405–428. DOI: 10.1016/0022-460X(77)90493-X.

Terracol, M. et al. (2023). "Numerical Simulations of a Landing Gear with Flow Through Fairings for Noise Mitigation". In: *AIAA AVIATION 2023 Forum*. American Institute of Aeronautics and Astronautics. DOI: 10.2514/6.2023-4173.

Turhan, B. et al. (2024). "Acoustic characteristics of phase-synchronized adjacent propellers". In: *The Journal of the Acoustical Society of America* 155.5, pp. 3242–3253. DOI: 10.1121/10.0025990.

Vries, R. de et al. (2021). "Aerodynamic interaction between propellers of a distributed-propulsion system in forward flight". In: *Aerospace Science and Technology* 118, p. 107009. DOI: 10.1016/j.ast.2021.107009.

Williams, J. E. Ffowcs and Hawkings, D. L. (1969). "Sound generation by turbulence and surfaces in arbitrary motion". In: *Phil. Trans. R. Soc. London A* 264.1151, pp. 321–342. DOI: 10.1098/rsta.1969.0031.

Zhe, Y., Meinke, M., and Schröder, W. (2024). "Numerical Analysis of Propeller-Airfoil Interaction in a Distributed Propulsion System Using a Hybrid LES and FW-H Approach". In: *30th AIAA/CEAS Aeroacoustics Conference (2024)*, p. 3211. DOI: 10.2514/6.2024-3211.